Coordination Chemistry Reviews 277–278 (2014) 208–223

Contents lists available at ScienceDirect

Coordination Chemistry Reviews

journal homepage: www.elsevier.com/locate/ccr

Review

Progress towards five dimensional diffraction imaging of functional materials under process conditions

Andrew M. Beale[a,b,*], Simon D.M. Jacques[c,d], Emma K. Gibson[a,b], Marco Di Michiel[e]

[a] Department of Chemistry, University College London, 21 Gordon Street, WC1H 0AJ London, UK
[b] UK Catalysis Hub, Rutherford Appleton Laboratory, Research Complex at Harwell, Harwell, Didcot OX11 0FA, UK
[c] MXIF, Rutherford Appleton Laboratory, Research Complex at Harwell, Harwell, Didcot OX11 0FA, UK
[d] School of Materials, University of Manchester, Manchester, Lancashire M13 9PL, UK
[e] European Synchrotron Radiation Facility, F-38000 Grenoble, France

Contents

ARTICLE INFO

Article history:
Received 6 February 2014
Received in revised form 9 May 2014
Accepted 10 May 2014
Available online 20 May 2014

ABSTRACT

In recent times there has been much progress in the imaging of functional materials under the process conditions typically used in a real industrial process. In this article the progress made in diffraction imaging in terms of both acquisition methodology (i.e. using white beam or monochromatic sources, tomography or imaging) and their application to tackle real problems in the field of industrial heterogeneous catalysis are discussed. The exemplar studies also illustrate the recent developments in sample environment that, when considered alongside the developments in diffraction imaging, allows us to

* Corresponding author at: Department of Chemistry, University College London, 21 Gordon Street, WC1H 0AJ, London, UK. Tel.: +44 01235 567837; fax: +44 01235 567779.
E-mail address: Andrew.Beale@ucl.ac.uk (A.M. Beale).

http://dx.doi.org/10.1016/j.ccr.2014.05.008

Keywords:
Diffraction imaging
Process conditions
Heterogeneous catalysis
Materials

propose that the information extracted from these studies are far more inclusive (conclusive?) in terms of the type (including physicochemical insight) and amount of information they yield. With the current and protracted developments in source, infrastructure, detector and software technologies it is not unreasonable to assume that such approaches will supersede the more traditional 'single point' in situ methods for studying industrial processes. Diffraction imaging methods in their various guises may also eventually replace the established technique of X-ray Absorption μ-CT currently applied intensively across research and diagnostic fields including biomaterials, geology, environmental science, palaeontology, cultural heritage and health.

1. Introduction

It has been long argued that in order for the results from characterisation studies of functional materials to have some industrial relevance they should be obtained under the 'relevant' reaction conditions i.e. under the same conditions as those used in an industrial process. The origins of this discussion can be traced back to the many and varied studies of catalytic reactivity at surfaces which tended to focus on well defined (polished) single crystals of pure elements during minimal (in terms of pressure and composition) gas atmospheres [1–5]. Despite the detailed behavioural and mechanistic insight gleaned from such studies (and Nobel prizes forthwith), the validity or significance of such approaches for obtaining better insight into the modus operandi of materials under process conditions has been questioned, often because the samples studied and the conditions used are often very different from those used in an industrial process. These 'gaps' in the study conditions have been accordingly labelled the 'materials gap' and the 'pressure gap' respectively and are well documented. In recent times there have been great strides made to bridge these gaps by developing apparatus (sources, setups and detectors) enabling the acquisition of data under more relevant reaction conditions [6–10]. About the same time that the materials gap and pressure gap came to the fore, a new term 'operando' was introduced to mean an experiment whose characterisation results could be correlated with some measure of materials performance – with catalysis in mind the aim is to correlate some evolving property of the catalyst (active phase) with performance (activity) [11,12]. Some protagonists in the field have sought to drive/define the ambitions of operando further by trying to mimic the exact conditions used in an industrial process and to perform the characterisation under these conditions [13]. This could conceivably be a third gap for in situ catalytic investigation i.e. to obtain data under the relevant reaction conditions in order to bridge an 'operando gap' [13–17]. This is not at all an easy gap to bridge since extremes of temperature, pressure and composition used in an industrial process often require that the reactor cell used comprises robust materials such as stainless steel which are not readily conducive to real time content interrogation by many of the spectroscopic/scattering techniques [13]. Furthermore there is the crucial issue of safety with the industrial process benefiting from many years of optimisation that the miniature improvised replicas used in laboratory studies do not have. Our fourth and final gap that we propose requires further attention is what we term the 'dimensionality gap'. The origin of this gap stems from the tendency for in situ and operando experiments to be performed at one point in the sample and that therefore they cannot consider spatial variation or the heterogeneity of catalyst composition/behaviour when trying to elicit important structure–function relationships. However, the improved performance of analytical apparatus (both sources and detectors) in recent times has seen a number of successful attempts at obtaining rapid time-resolved data (i.e. spectra, patterns) from multiple positions within a single sample or else from a sample ensemble via the performing of time-resolved imaging/tomography experiments [18–22]. Such 'chemical imaging' methods have reached a stage that enable the studying of functional materials in 5 dimensions i.e. obtaining spatially resolved (1D–3D) spectra/patterns from a sample as a function of time. This then is the background setting for this review which covers the recent developments/efforts that have been made towards 5 dimensional imaging focusing primarily and appropriately in 2014 this UN International year of Crystallography, on imaging methods that use coherent X-ray diffraction and scattering. Here the term imaging is used as an umbrella term covering two general data acquisition modes: radiography (2D mapping) and computed tomography (2 and 3D imaging). In practical terms X-ray diffraction and scattering imaging utilises microbeams that are rapidly rastered across a sample and at each point in this measurement protocol a pattern is acquired. Naturally for this method to be able to provide meaningful 5D data, pattern acquisition is typically rapid (~ ms/s per pattern) and therefore requires the use of bright X-ray sources (i.e. synchrotrons) and high performance area detectors. This arrangement is particularly advantaged by the use of very hard X-ray sources (>20 keV) which enables sample interrogation from within sometimes quite complex sample environments necessary to create the appropriate process conditions. The examples we have chosen to showcase here demonstrate what is now possible in terms of X-ray diffraction and scattering imaging of samples primarily focusing on their application in catalytic science but latterly we aim to demonstrate their potential for yielding insight into the behaviour of other types of functional material.

2. Methodology

2.1. Source

By virtue of their high penetrating power (high mean-free path), X-rays lend themselves readily towards the characterisation of samples under operating conditions. More often than not however a synchrotron source is required so as to be able to obtain multi-dimensional (imaging) data on the samples of interest. Synchrotron Radiation (SR) is very bright (>10^{10} photons s^{-1} $mrad^{-2}$ mm^{-2} 0.1%bw), highly coherent across a swathe of the electromagnetic spectrum (>0.1–140,000 keV) and typically produces well defined, intense beams on the sample (Fig. 1). This coupled with the availability of high performance detectors enables the recording of high quality data (i.e. high sensitivity and signal-to-noise) with exposure times per point (<μm) amounting to ms or less. X-rays are used to interrogate a sample by virtue of its tendency to absorb (emit) or scatter an incident photon in order to obtain for example elemental composition, local atomic coordination/oxidation state, crystallinity, density, etc.; Scattering and diffraction measurements in particular have routinely utilised SR for structure determination or else for in situ kinetic studies during phase transformation. In numerous cases however, it has been demonstrated that the behaviour of the sample under investigation is non-uniform.

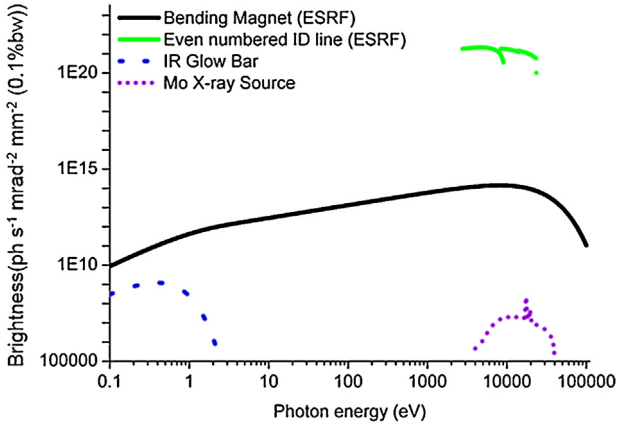

Fig. 1. Typical spectra (brightness against photon energy) comparing an IR glow-bar source, an X-ray tube (40 kV) with a Mo source and synchrotron radiation emitted by a bending magnet and by typical even numbered insertion device lines at the ESRF (6 GeV source, 200 mA current).

Recently a number of diffraction-based imaging methodologies have been developed that allow for the extraction of physico-chemical signals to be mapped from bulk objects either statically or else under process conditions [23–25]. Imaging techniques based on X-ray diffraction provide detailed atomic structural (reciprocal space) information from nm scale sampling volumes within samples having cm sized dimensions [26,27]. This combination of highly penetrating power of X-rays and focused beam enables one to study, for example, the in situ operation of individual catalyst particles/bodies instead of an ensemble of particles in a packed bed [13,28,29]. There are several advantages to using such methods: (1) the sample under study can be truly representative e.g. it can be taken from a stock of industrially prepared catalyst; (2) it can reveal spatial variations in chemistry or physical form i.e. does not assume homogeneity; (3) the sample can be readily separated from contributions from any enclosing cell or in situ apparatus; (4) interactions between spatially separated components can be investigated allowing the operation of devices fabricated from many materials to be studied.

2.2. Diffraction

Ordered materials can diffract X-rays at characteristic angles due to constructive interference phenomena between atomic planes. The diffraction condition is described by Bragg's law:

$$n\lambda = 2d\sin\theta \quad (1)$$

Here, n is an integer, λ is the incident X-ray wavelength, d is the distance between atomic planes (the desired variable), θ is the angle of incidence to a set of planes (2θ is the scattering angle). Two obvious routes exist to obtain d. One can fix λ by virtue of a monochromator, and scan 2θ, so called angle-dispersive diffraction (ADD); with the advent of modern 2D area detectors, 2θ is not scanned per se but is recorded in a single snapshot. An alternative route to determining d is by fixing 2θ using slits or a collimator to define a specific scattering path, and λ then becomes the scanned variable. In practice this is most commonly achieved using energy-discriminating detectors (making use of the known energy-wavelength relationship (2)) and is thus termed energy-dispersive diffraction (EDD). Bragg's law (1) can be rewritten to the energy-dispersive form (3). Both diffraction modes, angle and energy-dispersive diffraction, have their merits (e.g. energy-dispersive is additionally sensitive to elemental fluorescence) but the latter is generally less favoured due to its inherent poorer d-spacing resolution Δd. Nevertheless, both methods have been exploited for imaging purposes to obtain physio-chemical insight.

$$E = \frac{hc}{\lambda} \quad (2)$$

$$Ed\sin\theta = \frac{mhc}{2} \quad (3)$$

A schematic of transmission diffraction geometries for both modes is given in Fig. 2. In the angle-dispersive method diffraction contributions originate from all points along the incident beam path. With the energy-dispersive geometry scattering is recorded from a discreet sampling volume.

2.2.1. Pioneering diffraction imaging work

Harding et al. first demonstrated the potential of exploiting both these methods using a computed tomography approach. These initial studies employed laboratory based X-ray sources which possess a low flux [30–32]. Whilst such conventional sources are suitable for transmission based imaging such as radiography and by extension computed tomography they are not considered practical for diffraction imaging, where the measured signals are comparatively very weak. This necessitates extremely long data collection times (hours) to obtain reasonable counting statistics. We revisit this point further below. In contrast, synchrotron X-ray sources give very high flux and brilliance, and additionally offer tuneable wavelength resulting in much faster measurements allowing for obtaining data with a higher spatial resolution or else to image a sample as a function of time.

2.2.2. Developments in energy-dispersive imaging

Tomographic Energy Dispersive Diffraction Imaging (TEDDI) at a synchrotron was first demonstrated by Hall et al. [33–36]. Here the discreet scattering volume in the energy-dispersive geometry is used as a sampling probe, and the object under study is simply moved about this volume to build diffraction maps. The irregular (rhombus-shaped) nature of the scattering volume gives a large depth sampling leading to poor spatial resolution in one direction. A step scanning method to overcome this deficiency was developed by Lazzari et al. and more recently a modified computed tomography approach adopted whereby the object is swept through the diffracting volume under continuous collection to yield each projection [37,38]. Since these studies focused on method development static objects or else objects under steady-state conditions were used to obtain 1D or 2D spatially resolved data. Attempts at time-resolved studies have also been made successfully yielding both 2D (1D space + 1D time) and 3D (2D space + 1D time) insight into the chemistry in an evolving system [39,40]. A weakness of the TEDDI incarnation has generally been the use of a single-point energy-discriminating detector for collection i.e. only a small solid angle of the sphere of diffracting signal is collected. The corresponding low statistics, even when employing powerful white sources, has effectively ruled out large size 2D (images composed of a high number of pixels) or 3D volume studies. The benefits of sampling a greater portion of scattering is perhaps illustrated in the use of both rasterised angle-dispersive diffraction and TEDDI in a high-energy X-ray study by Middelkoop et al. where the radially integrated angle-dispersive data gives rise to patterns with good statistics despite the fact that only a narrow monochromatic band of radiation was used for these measurements [41].

2.2.3. Developments in angle-dispersive imaging

A number of studies made use of the raster scanning angle-dispersive method [13,29,42,43]. The main problem with such studies is the lack of a depth contrast from the sample since there are diffraction contributions originating from all points along

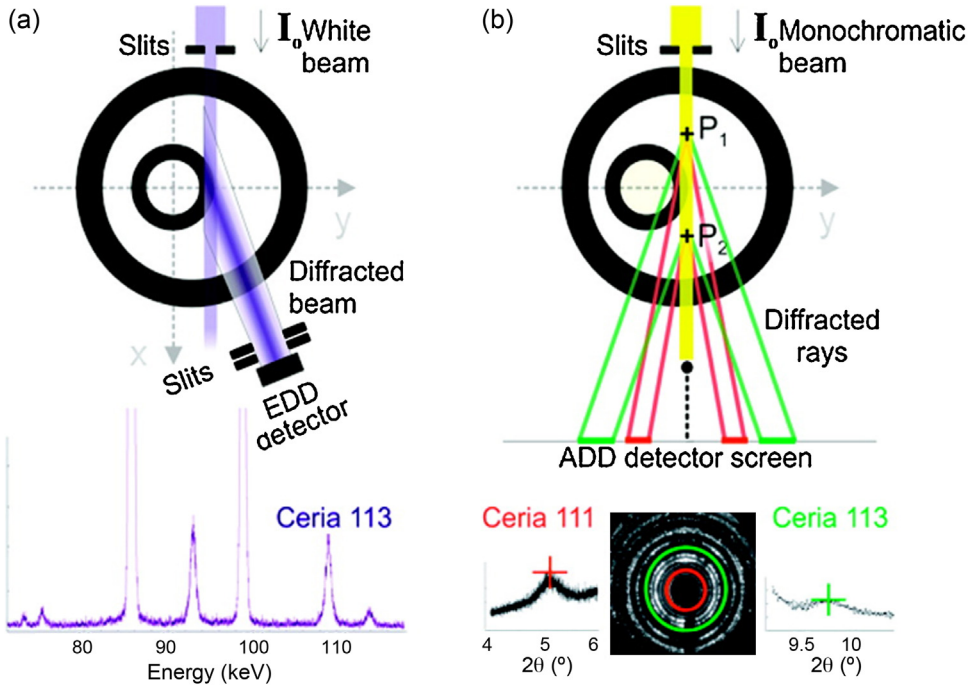

Fig. 2. Schematic illustrating the principles of (a) Energy Dispersive Diffraction (EDD), showing diffraction from a discrete volume (a small, thin-walled stainless steel tube inside a larger thicker-walled tube), defined by the incident and diffracted beam slits, detected by an energy-discriminating device; a well-resolved energy-dispersive diffraction pattern is shown beneath with the position of, for example, the ceria (1 1 3) reflection indicated. (b) Angle Dispersive Diffraction (ADD) setup, from different reflections at different points within an object recorded on an area detector. Below are shown (highlighted in red and green) the Debye–Scherrer rings from the ceria (1 1 1) and (1 1 3) reflections. Note that the data collection volume and time is greater in the EDD case thus resulting in data with better signal-to-noise. Reprinted with permission from Middelkoop et al. Chem Mater. 21 (2009) 2430–2435. Copyright 2009 American Chemical Society.

the incident beam path (including air scatter and any apparatus). Tomography methods such as XRD-CT overcome this problem, the technique being first demonstrated on a synchrotron facility by Bleuet et al. adopting Hardings original CT approach [23,30]. This study has since spawned a number of subsequent XRD-CT studies that mainly yielding 2D information [24,44–46]. However, a major reduction in speed of collection has been achieved through optimisation of beam defining optics and use of modern high speed detectors which has enabled 3D studies, either dynamic 2D or indeed 3D spatial [47,48]. This and other work has recently been reviewed by Alvarez et al.; this paper also discusses some of the practical issues with the XRD-CT method [24]. Most recently Egan et al. reported a study where each collected diffraction pattern was obtained in 66 ms, producing 100 × 100 images (150 μm resolution) now akin to what could be collected by conventional pencil beam μCT [49].

2.2.3.1. Collection and processing of XRD-CT data. XRD-CT experiments are normally performed using a micro pencil beam some 2–100 μm^2 with the resultant diffracted X-rays recorded on a flat panel detector. In a typical experiment a 2D cross-section is first mapped (i.e. a pattern is recorded for <1 s) by translation of the sample perpendicular to the beam in steps equivalent to the beam width. The sample is subsequently rotated and the translational mapping repeated. This entire process is repeated several times until the sample has been rotated by at least 180°. The resultant powder ring data are then radially integrated (using radial integration software such as Datasqueeze, XRDUA and a well characterised crystalline material such as CeO_2 or LaB_6 as a calibrant) for each measurement performed [50,51]. Often it is this step that is rate determining in the analysis as the outputted image files from the 2D area detectors are rather large (~8 MB) and a 2D slice may comprise a few thousand patterns. For each observed intensity value (I_{OBS}) in the radially integrated or 'squeezed' patterns (i.e. for all 2θ's) a sinogram is constructed and then back-projected via a suitable algorithm to a square pixel image where each pixel comprises a full diffraction pattern. As a result for N values of 2θ, this yielded N real space reconstructed images. It follows that any vector perpendicular to such a stack of images will yield a reconstructed diffraction pattern corresponding to the selected volume element in the slice. Typically 2D intensity distribution maps are produced using 'diagnostic' reflections (this can be raw or else fitted intensities although it can also include Full Width at Half Maximum (FWHM) and peak position) from for the crystalline phases present. The analysis and visualisation of this considerable volume of diffraction data requires therefore the development of dedicated software capable of batch data processing. However in some instances the data are of sufficient quality that detailed parameter maps could equally be produced by using a Rietveld phase scale factor or else a map of lattice parameter variation and potentially occupancy and thermal factors [49]. The entire data processing approach is given in Fig. 3.

2.2.4. Pair distribution function imaging

These studies have been limited to studying materials that exhibit high crystallographic ordering, that is, the methods fail to provide physico-chemical insight into materials that are not highly crystalline [52]. Elemental characteristic fluorescence signals as available when employing energy-dispersive detectors provide some compositional insight but the major recent advance to address this deficiency is the development of Pair Distribution Function (PDF) Computed Tomography which uses both the Bragg and diffuse scattering signal to characterise both nanocrystalline and classically considered amorphous materials [53]. The Pair Distribution Function $G(r)$ is arrived at through the sine Fourier transform of the total scattering function $S(Q)$ and represents the probability of finding an atom at a given distance, r, from

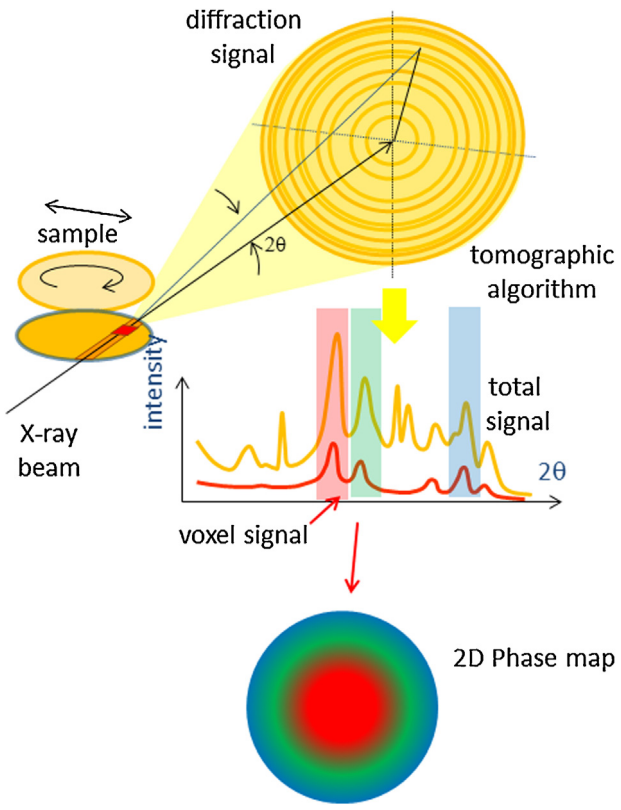

Fig. 3. Illustration of the sampling methodology used to obtain representative 2D cross-sectional XRD-CT data from a sample. Essentially the process involves a data acquisition step (a few min per 2D slice), radial integration to give a 1D pattern (yellow arrow), feature selection/fitting (coloured rectangles are used to identify different diagnostic features) and finally sinogram construction and filtered back projection of these various features to yield their 2D distribution.

another atom. The relative intensity in the PDF relates directly to the number of these atom pairs and their scattering power.

$$G(r) = \frac{2}{\pi}\int_{Q_{\min}}^{\infty} Q[S(Q)-1]\sin QrdQ \quad (4)$$

For nanostructured materials, the intensities of the PDF peaks diminish with increasing r due to the finite size of the objects (or more strictly the finite range of the structural coherence). The point at which peaks disappear in the PDF can, in some instances, be used to determine the largest extent of the structural order in the material and therefore be used to ascertain whether a material is amorphous or nano-crystalline (or indeed highly crystalline). From an imaging perspective this method has very recently been demonstrated to map amorphous, nano-, and highly crystalline material in bulk objects, including the nano-crystalline state and size of an industrial catalyst under in situ conditions [53]. The PDF method requires capture of a large Q space range and since X-ray scatter falls off as a function of $\sin(\theta)/\lambda$ one must have reasonable counting statistics at high Q to obtain useful PDF. It can be argued that the PDF-CT incarnation of XRD-CT is count limited by the narrow bandwidth of radiation used (typically 0.1 or 0.2% bandwidth is used for PDF studies). Whilst there is scope for using broader band radiation for PDF work, with the generally accepted upper limit of 0.5% bandwidth, this becomes increasingly less useful for nano crystalline materials.

2.3. Source and detector performance

2.3.1. Advantages of a bright hard energy source

Diffraction imaging experiments are performed in transmission mode. The best results are often obtained on undulator beamlines at high energy 3rd generation synchrotron sources. In addition to a high photon flux, the number of photons that reach the detector depends also upon sample absorption. The transmission (I/I_0) through the sample (s) and reactor (r) determines the number of photons detected per unit time at the detector. This is calculated from the Beer–Lambert law using the attenuation coefficient of the materials (μ) (determined by mass attenuation coefficient and density), their thickness (t) and the volume fraction which the sample occupies (v):

$$I = I_0 \exp(-(\mu s * ts * vs + \mu r * tr * vr)) \quad (5)$$

The advantage of using very hard X-rays, is that X-ray transmission is still significant in thick samples. This greater transmission then allows for interrogation of both thicker and denser materials akin to the types of reactor used in industrial catalysis.

There are however some drawbacks with performing these types of measurements. Firstly by using higher energies although transmission is higher there is less X-ray elastic scattering (smaller cross section) seen at higher energies [13]. In addition a higher signal-to-noise ratio is achieved, per unit time, allowing for faster sample interrogation. Care must still be taken to consider the effect of tan 2θ sample broadening (β_{samp}) in the scattering signal which (at a fixed d-spacing) is a function of both energy (in the 2θ term) and sample thickness (t):

$$\beta_{\text{samp}} = t\tan 2\theta \quad (6)$$

Additional advantages of using harder X-ray sources include a larger Compton cross section allowing for the collection of the inelastically scattered signal and an increased Ewald sphere radius at higher energies (i.e. shorter wavelength (λ)). This results in a compression of the scattering vectors into a smaller 2θ range, providing more data on the sample of interest as more reflections can be observed. For PDF-CT experiments acquisition of scattering data over a large 2θ or q-range is a must so as to obtain sufficient resolution to identify scattering pairs without ambiguity. The compression of many scattering vectors into the limited pixel range of a detector does however result in a decrease in the peak resolution, which can impact upon data analysis (i.e. a Rietveld analysis), although this problem can in some cases be mitigated by decreasing the recorded 2θ range (increasing the sample-detector distance). In essence it is possible to now exact choice between a larger Δq vs. higher peak shape resolution.

2.3.2. Detector performance

Making use of a much broader band of the source, requires either the use of energy sensitive detectors or analyser technology (i.e. post sample monochromators) coupled to standard 2D intensity recording devices. The latter does not provide a realistic route to increased speed of collection whilst the energy sensitive detectors have traditionally been small area detectors or large slab detectors effectively used as single point detectors [54,55]. However, more recently there has been a drive to develop pixelated devices with energy-sensitivity. This has included the development of multispectral (pixelated) devices which, whilst possessing a reasonable number of pixels, generally offer relatively poor energy resolution relying on a number of comparator levels rather than recording a continuous spectral image [56–58]. However, pixelated devices offering the prospect of good energy resolution over a range of 30 keV have been reported [59–61]. Most recently a 80×80 pixel camera system supporting real-time hyperspectral X-ray imaging

up to very high energies (~150 keV) has been reported; the technology is in the process of being extended to larger pixel devices [62]. Such detectors offer new chemical sensitive imaging capabilities such as white beam diffraction radiography and computed tomography [63,64]. In the latter of these studies the sample is illuminated with a flood field of white X-rays and the diffraction signal is projected through a pinhole. Whilst this is a simple configuration, only a tiny portion of the scattered photons are collected and perhaps this technique will be best able to be exploited with pinhole arrays or coded apertures, for example applying a modified form of that previously described [65–67]. Pixelated energy-dispersive cameras also offer the prospect for development of PDF recording and PDF imaging, though studies have yet to be reported.

We have thus far considered two properties of scattered light, i.e. intensity and wavelength (energy) but one can also consider other properties such as phase, direction and polarisation. Certainly phase information has been extracted and exploited to improve traditional radiography and computed tomography, so called phase contrast methods [68,69]. Indeed a recent theoretical paper showed the possibility of one-shot phase retrieval from energy-sensitive pixelated devices where in principle several phase images should be available from the energy domain of a hyperspectral camera [70]. Of perhaps much greater potential is to obtain the direction of scattered photons since the imaging techniques above require explicit or some knowledge of the origin of the photons. If fast detectors with energy and direction sensitivity could be constructed then a large portion of the scattered photons could be collected from a sample flood-field illuminated with white X-rays. Such a system would open up the possibility of real time 5D imaging at bright sources such as synchrotrons and would offer the prospect of high dimensional imaging in the laboratory.

3. Sample results

Dynamic imaging studies to date have capitalised on the brightness available at 3rd generation synchrotron sources to deliver μm beams that enable the 'chemical' mapping of mm-sized objects over a spatial dimension of a few mm within a time period of a few minutes (<10). This then is readily sufficient to observe solid-state transformations and is therefore where the real value of the application of these techniques lie. In what follows we detail a series of experiments in the form of a chronology of the lifetime of an industrial catalyst from its inception (synthesis of a crystalline support phase) to its eventual deactivation via degradation as a result of poisoning. This is then followed by a look at one or two other studies on functional materials to illustrate the scope for diffraction imaging techniques applied in a time-resolved manner.

3.1. Catalyst preparation

3.1.1. Synthesis of a catalyst support

CeO_2 is a common catalyst support material, particularly favoured in three-way catalyst formulations providing both a robustness and redox functionality [71,72]. In recent times there has been an interest in providing high surface area CeO_2 materials with methods that utilise supercritical conditions and are therefore capable of producing large volumes of material [73]. Critically the properties (size, shape, etc.) and therefore the performance of CeO_2 can be influenced by the process conditions used to prepare it but without being able to observe the formation process in real time it is difficult to understand the origins of this relationship [74]. For this purpose Middelkoop and collaborators used high energy X-ray diffraction to study the formation of nanoparticulate CeO_2 within a continuous hydrothermal flow synthesis (CHFS) reactor [41]. High energy X-rays were required to penetrate the steel CHFS apparatus which essentially utilised an inner stainless steel tube (3.2 mm OD) to deliver super-critical water (450 °C, 22.1 MPa) to a stream of cold cerium ammonium nitrate solution (20 °C, 22.1 MPa in 9 mm OD stainless steel tube) [75]. A combination of raster scanning angle-dispersive (E = 89 keV) and energy-dispersive (E = 30–300 keV) was used to monitor the steady-state formation of nano-crystalline material in different regions of the reactor. By performing an intensity and peak width analysis of the forming CeO_2 it was possible to identify nucleation and growth zones within the reactor; a TEM analysis of outflow formed material was used to verify the particle size determined from an analysis of the XRD data. The authors subsequently used ADD alone to further investigate the growth and nucleation within a counter current CHFS reactor (with symmetric design) at three operating conditions (350, 400 and 450 °C at 24 MPa) [76]. The results showed that the typical particle size of the CeO_2 exhibited a small increase with increasing temperature as well as demonstrating that good agreement with behaviour of the reactor from modelling [77]. The work in these and other studies by the group, demonstrate how XRD imaging methods actually allow for a more detailed understanding of crystallisation processes, particularly since it is now possible to relate phase or physical property with some variation in a chemical process; such a variation (or its significance) would likely be missed when performing single point measurements [78].

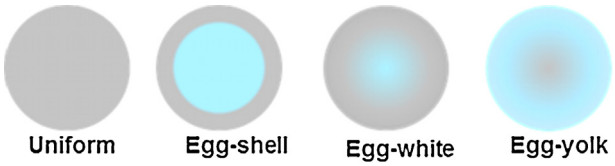

Fig. 4. A schematic description of the micro-distributions of an active phase in a cylindrical extrudate as observed when bisected. Note grey colour = active, blue colour = support.

3.1.2. Impregnation of a catalyst body

The majority of the dynamic imaging studies discussed focus on studying pre-shaped catalyst bodies ranging in size from a few um (~20 μm) to a few mm (5.5 mm) in size since they are used in many industrial catalytic processes. Their primary role is to minimise any pressure drop along the height of the reactor vessel. They comprise metals, metal oxides, carbides, and sulphide actives dispersed on high surface area supports (i.e. γ-Al_2O_3, SiO_2, TiO_2) often in the presence of various promoters [79,80].

The challenge for the catalyst manufacturer is to obtain high loadings of the active species with the required unique active phase–support interactions to produce an efficient (in terms of activity, selectivity, and stability) catalyst. The classical preparation method for industrial catalysts includes incipient wetness impregnation and drying followed by a thermal treatment [81,82]. In some cases, an additional chemical activation step is required, i.e. reduction or carburisation. Incipient wetness impregnation is performed under ambient conditions and relies on capillary forces inside the pores to draw the solvent throughout the internal volume of the particle resulting in a high dispersion of the active phase; uptake of the precursors into and onto the support is therefore diffusion limited. Impregnation is followed by an equilibration and drying time that ensures that the precursor solution reaches an equilibration distribution over the particle. Depending on the relative importance of time, porosity, pH and chemical speciation, different macrodistributions of the active species along the catalyst bodies can be obtained. In general, four distributions are defined, which are known as uniform, egg shell, egg yolk, and egg white (see Fig. 4).

To date X-ray absorption μ-CT has been used primarily to study the impregnation step since the catalyst precursor tends to lack

sufficient order to be seen by diffraction/scattering techniques [21,83–86]. The motivation for studying the impregnation process is ideally to determine the state of the precursor (as has been previously shown with spectroscopic techniques such as MRI, UV–vis and Raman spectroscopy), but also to follow the evolution and diffusion of the initial/final precursor as a function of 2D space [81,87,88]. The advantage with X-ray absorption μ-CT is that it is extremely fast with acquisition times in 2D of ms and in 3D in s but this is only achievable due to a lack of 'chemical' contrast which renders the technique blind to the evolving chemical processes at play in the systems under study. In simple or well-studied systems however it is possible to rationalise the X-ray absorption μ-CT when additional/complementary spectroscopic information is also available. Inclusive of these studies has been catalyst impregnation and in particular a study of the effect of immersion time upon the ingress of $CuCl_2$ in solution within γ-Al_2O_3 pellets [21]. Immersion times of 1 min, and 10 min were used with the acquired data from the study and enabled for the clear observation of movement of a diffusion front towards the centre of the pellet. However, the thickness of the impregnated part exhibited radial and axial variation, most likely caused by a variation in the pellet structure as a result of the extrusion process.

In a second, more recent example, X-ray absorption μ-CT was used to follow the 3D evolution of Mo species inside a 3 mm γ-Al_2O_3 extrudate during impregnation and the subsequent drying stage [89]. Of particular note here was that whilst Mo is initially uniformly distributed over the catalyst body, in time hot spots were observed to grow in number and size as more Mo diffuses through the pellet. The authors were able to perform an analysis of the pixel volumes determining parameters such as hot spot size and shape which could then be used to extract kinetic and mechanistic insight into the hotspot growth process revealing that a minimum Mo concentration is required before nucleation occurs. Growth however, once started, is initially rapid, followed by a slower period possibly due to agglomeration and eventually a 'final' fast step possibly due to the coalescence of adjacent hotspots. This entire process is radically accelerated by drying of the sample. Separate Raman microspectroscopy measurements allowed for rationalising the chemistry behind the hot-spot formation and in particular the formation of AlMoly species via the reaction detailed below [7]:

$$12Mo_7O_{24}^{6-} + 7Al_2O_3 + 27H_2O + 30H^+ \rightarrow 14Al(OH)_6Mo_6O_{18}^{3-} \quad (7)$$

The formation of these hotspots can be arrested by co-impregnating with H_3PO_4 and leads furthermore to a uniform distribution of Mo during impregnation (see Fig. 5). However the drying step was shown to be responsible for the migration of Mo species to the periphery of the extrudate (see Fig. 4 from 17 min. onwards). Again separate Raman spectroscopic measurements needed to be performed on the samples in order to determine the chemistry behind the cause of the Mo distribution, in this case the formation of $H_xP_2Mo_5O_{23}^{(6-x)-}$ which does not bind strongly to the Al_2O_3 support and thus is quickly removed with the solvent on drying.

A detailed kinetic evolution of aluminium molybdate formation and growth was only possible in this study by using a combination of X-ray absorption μ-CT and Raman spectroscopy. This requires performing the exact same experiment twice (using two different analytical techniques) in the anticipation of obtaining the same result (one can reasonably assume here that the results are reproducible). It is rare to be able to perform two separate in situ experiments under the exact same conditions with this study illustrating nicely some of the problems of performing two separate studies; for example, whilst X-ray absorption μ-CT was performed in an in situ manner, Raman microspectroscopy was performed in the traditional 'cut and measure' approach leading to shorter impregnation and faster drying step and therefore leading to quicker AlMoly formation. Although it is possible to perform non-invasive Raman spectroscopy on a sample in a reactor environment and to obtain spatially resolved data it is not always possible to perform two separate measurements that require challenging experimental conditions, particular high pressures [90].

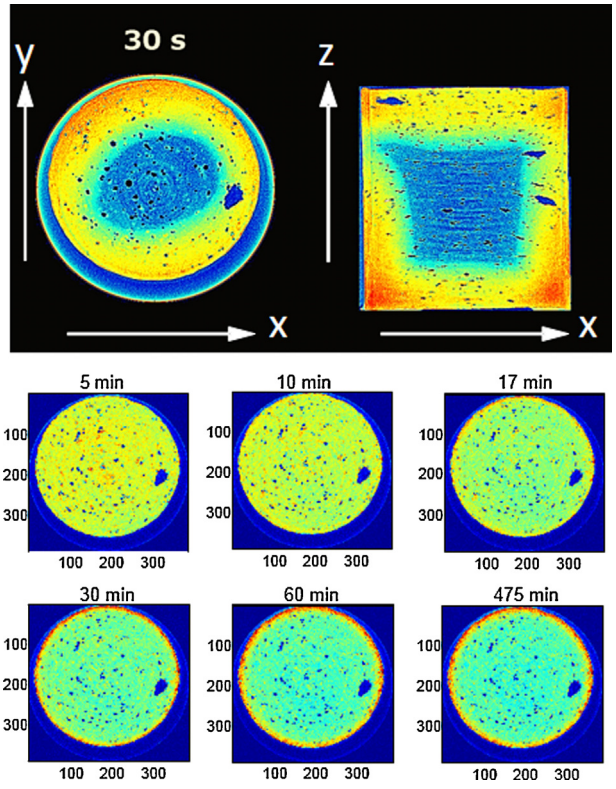

Fig. 5. (top) 2D X-ray absorption μ-CT *xy* and *xz* images of a slice of a γ-Al_2O_3 extrudate after incipient wetness impregnation of a 1.3 M Mo ammonium heptamolybdate solution containing 0.65 M H_3PO_4 at pH 2 after 30 s equilibration time. (Bottom) X-ray absorption μ-CT *xy* cross-sections of a γ-Al_2O_3 extrudate after incipient wetness impregnation of a 1.3 M Mo ammonium heptamolybdate solution containing 0.65 M H_3PO_4 at pH 2 as a function of time of drying in air at room temperature. Reprinted with permission from Gibson et al. ACS Catal. 3 (2013) 339–347. Copyright 2013 American Chemical Society.

3.1.3. Drying stage

The molecular precursors observed to form during the impregnation and drying of Mo/γ-Al_2O_3 are normally not ordered enough to be observed using XRD [87]. However, TEDDI is not limited to obtaining scattering information since it utilises a white beam and energy dispersive detector and thus also yields element composition (XRF) information for elements where $Z > 14$. Provided at least one unique 'diagnostic' peak can be identified for each crystalline phase/element present TEDDI offers a means of obtaining concentration maps for a number of crystalline phases and elements within a catalyst body in a time and space resolved manner. The fact that a full spectrum can be obtained from each voxel in the sample containing both diffraction and elemental composition information renders the technique useful for sample interrogation even when the material lacks long range order. Fig. 6 shows a typical detector response from a 'pixel' from a dried Mo/γ-Al_2O_3 catalyst body (1.5 mm $\phi \times$ 10 mm l). The broad background in the centre of the pattern attests to the lack of crystalline order in the sample (γ-Al_2O_3 phase (reflections at 67 and 78 keV) whilst the peaks to the left correspond to fluorescence of molybdenum (ca. 17.4 ($Mo_{Ka1,2}$) and 19.6 keV (Mo_{Kb})) ($[Al(OH)_6Mo_6O_{18}]_3$). The distribution of these signals in the *z*, *y* direction obtained from peak profiling point to the formation of an egg-shell distribution of MoO_3 (Fig. 5d) and a catalyst that was not effective for HDS activity. The cause of this

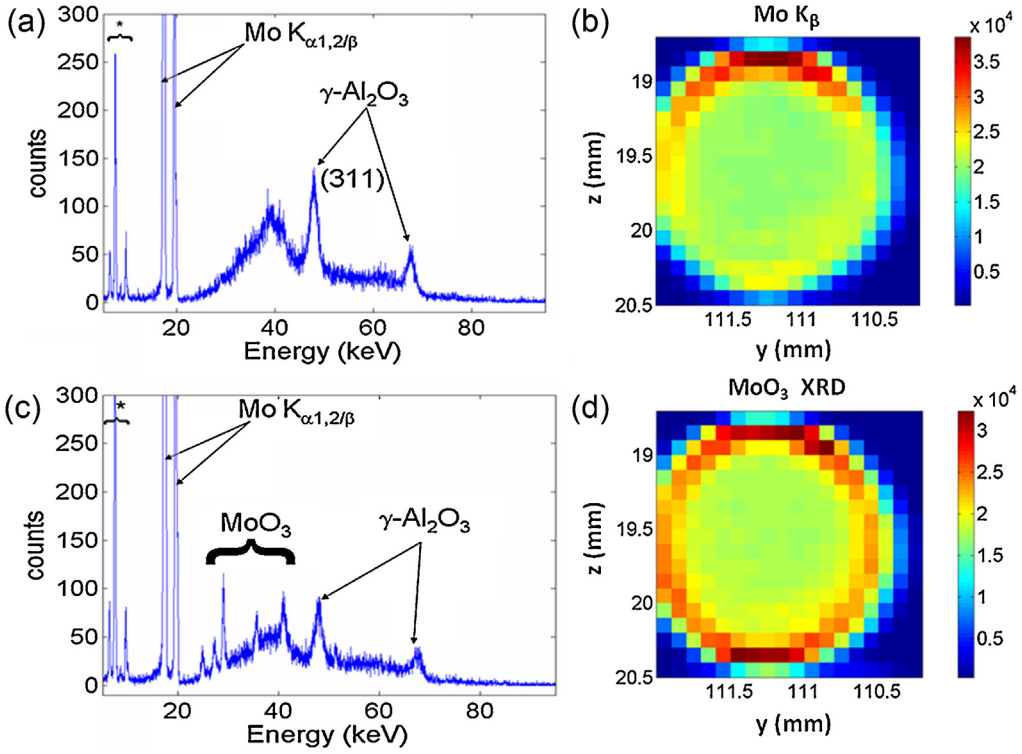

Fig. 6. (a) Detector signal from a Mo/Al_2O_3 catalyst body after drying at 120 °C (* represents the Ge detector escape peaks). (b) A typical *y*–*z* $Mo_K\alpha_{1,2}$ fluorescence map from the same catalyst body as in (a). The red (darker) areas represent regions in which the signal and therefore the species of interest are most concentrated. (c) Detector signal from a Mo/Al_2O_3 catalyst body after calcination at 500 °C. (d) A typical *y*–*z* diffraction map from the same catalyst body as in (a). Reprinted with permission from Beale et al. Angew. Chem. Int. Ed. 46 (2007) 8832–8835. Copyright 2007 Wiley-VCH.

'egg-shell' distribution was proposed to be either due to insufficient equilibration time during impregnation step or due else to a too high a concentration of molybdenum used. Co-addition of Co also yielded a catalyst lacking long range order with the 2D cross-sectional scans revealing *a* broadly even distribution of these elements over the sample. Down the length of the sample however it appeared a different matter with various 'hot spots' discovered implying a build-up of the active components at specific parts of the extrudate, although it was not clear why the build-up occurred specifically at these positions. This however maybe again related to variation in the internal structure of the pellet [35].

3.1.4. Calcining catalysts

A heat-treatment step of a catalyst body always precedes catalyst application since it is during this stage that the required crystalline metallic, metal-oxide, metal-sulphide, etc. phase for catalytic application forms. Both TEDDI and XRD-CT have been employed to follow the calcination process of Ni impregnated cylindrical 3 mm × 3 mm γ-Al_2O_3 catalyst body [40,47]. For both sets of experiments specially designed in situ cells were constructed that allowed for controlling the sample environment; in both cases requiring heating of the sample in an inert atmosphere. The main difference between these two setups is that the setup used for XRD-CT is more similar to a catalytic reactor whereas the setup used in the TEDDI experiments possesses a large dead volume and hence was termed an environmental cell. Shown in Fig. 7, are the results from the calcination from the TEDDI experiment – in this case the experiment is performed as a line scan through the centre of the catalyst body. 2D maps of the sample (not shown) revealed that the initial $[Ni(en)(H_2O)_4]Cl_2/\gamma$-$Al_2O_3$ sample after impregnation and drying contained no Ni containing crystalline phases although Ni fluorescence maps revealed the Ni to be distributed mainly at the sample edges (Fig. 7). In the early stages of calcination in N_2 an unknown crystalline precursor forms (~150 °C) which whilst yielding the desired final face centred cubic (fcc) Ni phase, does so via a number of additional intermediate steps, including the formation of a second unknown phase, followed by what appears to be either Ni_3C or hexagonally close packed (hcp) Ni and finally crystalline fcc Ni (from ~350 °C). A lack of resolution meant that it was not possible to unambiguously determine the presence of Ni_3C and/or hcp Ni so the authors used chemical intuition (based on the presence of large amounts of amorphous carbon in the sample) to initially assign the peaks to the Ni_3C phase. Interestingly both 2D *yz* and the dynamic *xy* scans revealed significant differences in the phase composition across the sample: for example in the core of the pellet Ni_3C is the predominant phase (accounting for ~40% of the total Ni present), whilst at the edge this amounts to less than 20% – the remainder comprising fcc Ni. As the dynamic *xy* scans revealed, fcc Ni is the only crystalline Ni phase present on reaching 460 °C and possessed an average particle size was of the order 24–34 nm; the large Ni particles likely created as a result of promotion of crystal growth by Cl anions. Although the study could not provide mechanistic insight into the phase evolution process, it revealed that the formation of an active component is a multi-step evolution process showing significant spatial variation.

Improving the acquisition time and data quality in order to obtain more detailed solid-state insight into the evolving solid-state chemistry was the motivation behind the development and application of X-ray diffraction computed tomography, XRD-CT [47,53]. Whilst TEDDI images a sample by the process of mapping, XRD-CT requires the use of a mathematical algorithm to construct an image out of XRD projections. With respect to a typical TEDDI experiment, XRD-CT yields better quality data both more quickly (measurement time of ms instead of s) and with a higher spatial resolution (≤100 μm vs 100–1000 μm). The gas tight environment in this case consists of a quartz cell and gas delivery stub. The latter

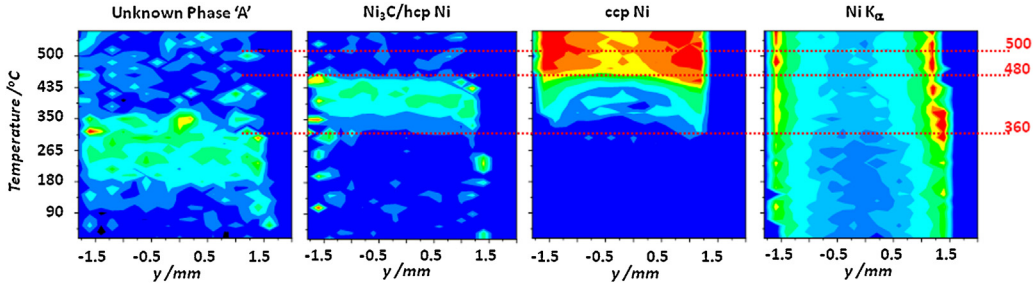

Fig. 7. Y scan maps as a function of temperature during calcination of $[Ni(en)(H_2O)_4]Cl_2/\gamma\text{-}Al_2O_3$ of a diffraction peak corresponding to an unknown Ni-containing crystalline phase (labelled 'A'), the (101) reflection assigned to Ni_3C, the (200) reflection of metallic fcc Ni, and the Ni K_α fluorescence line. The red colour represents regions where the concentration of the corresponding Ni species is the highest. Reprinted with permission from Espinosa-Alonso et al. J. Am. Chem. Soc. 131 (2009) 16932–16938. Copyright 2009 American Chemical Society

was fixed to a goniometer attached to a rotation stage. The entire set-up was itself mounted upon a translation stage, onto which were also mounted two heat guns; this allowed for translation of the heating guns with the sample.

By virtue of delivering XRD data of higher quality, XRD-CT was able to verify the observations made in the previous TEDDI study but that crucially not one but the two initial crystalline phases form at the beginning of calcination around 100–125 °C possessing a similar diffraction patterns but a different spatial distribution. The phases comprise an $Ni(en)_xCO_3$ phase (green) at the periphery (egg-shell) and $Ni(en)(CO_3)_xCl_{2(1-x)}.xH_2O$ phase (cyan), which possesses an egg-white distribution. The former ($Ni(en)_xCO_3$ phase) decomposes at ca. 325 °C leading to the first 'appearance' of the fcc Ni phase possessing the same egg-shell distribution (Fig. 8). The $Ni(en)(CO_3)_xCl_{2(1-x)}\cdot yH_2O$ phase on the inside of the pellet undergoes dehydration at ca. 175 °C yielding $Ni(en)(CO_3)_xCl_{2(1-x)}$ (yellow phase), followed by CO_2/en loss at ca. 300 °C to form $Ni(en)_{0.5}(O)_xCl_{2(1-x)}$ followed by 'O' and en loss from ca. 325 °C via a disproportionation reaction to yield $Ni(en)Cl_2$ and hcp Ni. Hexagonal close packed Ni was incorrectly assigned to Ni_3C in the previous TEDDI experiments, but now with the superior resolution of XRD-CT it could be unambiguously assigned to hcp Ni. Above 400 °C, $Ni(en)Cl_2$ and hcp Ni phase disappear to yield fcc Ni, which is uniformly distributed across the entire sample by 500 °C [40]. The data recorded from these measurements were also of sufficient quality so as to be able to extract additional structural information. In particular, a Scherrer analysis of the full-width at half maxima (FWHM) of the (220) fcc Ni reflection revealed that at slice 18, smaller crystallites of fcc Ni appeared in the centre (*vis.* larger crystallites seen at the cylinder periphery), reflecting the lag in phase growth in this region. At slice 22, whilst the pellet contains a uniform phase distribution, the crystallite size distribution is uneven; larger crystallites (~24 nm) are observed on the *inside* (egg-white) rather than towards the rim. The larger particles form where appreciable amounts of $Ni(en)Cl_2$ were previously observed, suggesting that chlorine promotes particle sintering/growth. $Ni(en)Cl_2$ is not seen at the periphery since the initial crystalline phase that forms there, ($Ni(en)_xCO_3$), does not contain Cl. By performing a series of 2D cross-sectional scans down the length (*z*-axis) of the catalyst body after calcination it was possible to obtain a 3D picture of the fcc Ni distribution over the catalyst which served to illustrate that the larger catalyst particles possessed a dumbbell-shaped distribution with fewer of these particles concentrated in the middle of the particle with respect to either end [47].

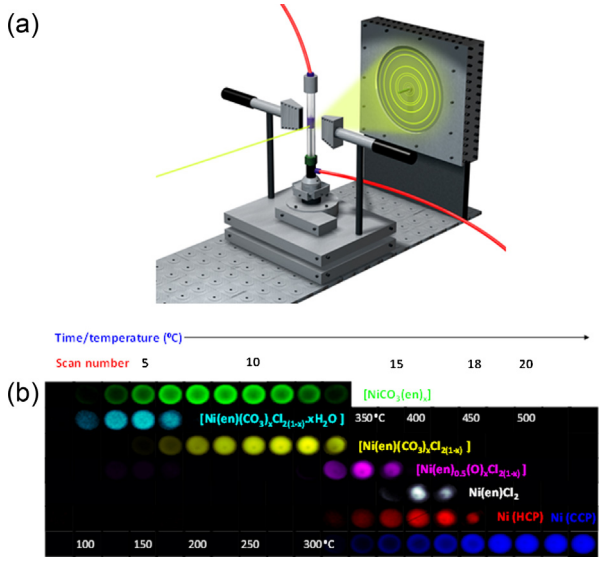

Fig. 8. (a) The 3 mm diameter × mm $\gamma\text{-}Al_2O_3$ catalyst body is mounted on an alumina rod, which is vertically aligned to rotate on the vertical axis with minimal precession. This is mounted in a plug-flow arrangement within a quartz capillary, either side of which are heating guns. XRD-CT imaging data are then collected in transmission mode. (b) The colour maps indicate the following distribution of solid-state phases accordingly: $Ni(en)_xCO_3$ (green), $Ni(en)(CO_3)_xCl_{2(1-x)}.xH_2O$ (cyan), $Ni(en)(CO_3)_xCl_{2(1-x)}$ (yellow), $Ni(en)_{0.5}(O)_xCl_{2(1-x)}$ (magenta), $Ni(en)Cl_2$ (white), hcp Ni (red) and fcc Ni (blue). Reprinted with permission from Jacques et al. Angew. Chem. Int. Ed. 50 (2011) 10148–10152. Copyright 2011 Wiley-VCH.

3.1.5. Linking preparation with activity

Structured metal catalysts, formed by an active catalyst layer deposited on a structured support such as a honeycomb, plate, foil or foam, possess a number of advantages over pelletised catalysts including lower pressure drop across the bed, a higher mechanical strength and a large geometric surface area. Furthermore their greater heat transfer capacity minimises thermal gradients and hot spots. A key challenge however to their utilisation is the coating of the active on the support so as to ensure good performance and stability. Conventional washcoat methods have been compared with an electrochemical deposition (ECD) methods for the production of a steam reforming catalyst (Ni/Al_2O_3) on a metallic FeCrAlY support in a recent publication by Basile et al. and the resultant coatings characterised in terms of both structure and chemical composition using a combination of combined XRF, X-ray powder diffraction tomography measurement and separate absorption tomography [91]. The combined μ-XRF and μ-X-ray powder diffraction (μ-XRD) were performed at 25 keV with a beam 3.4 × 1.8 μm in size with the μ-XRF data being collected using two Vortex silicon drift detectors at 90°.

Initial X-ray absorption tomography data for the ECD sample revealed the foams to be both hollow yet containing a thin layer of Al_2O_3 at the surface which provided the anchoring points for the active phase. Corresponding μ-XRF data shown in Fig. 9b revealed that the metallic FeCrAlY support comprised predominantly well

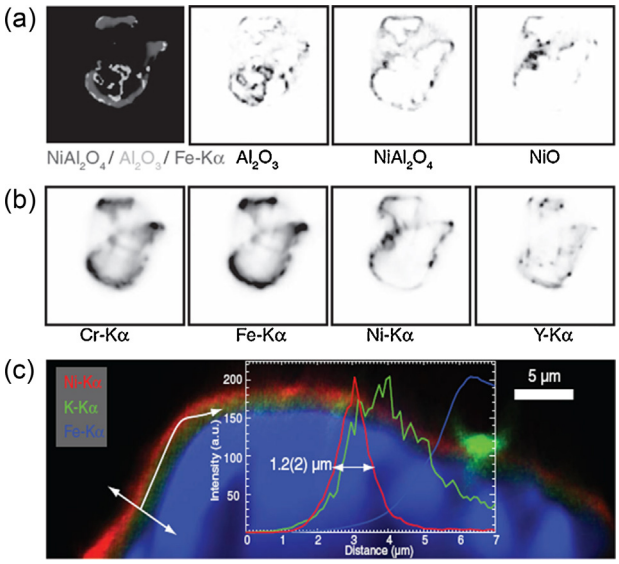

Fig. 9. (a) Diffraction phase maps created from diagnostic diffraction peaks obtained by XRF/μ-XRD-CT measurements. (b) Corresponding XRF maps. (c) Colour elemental maps of Ni, K and Fe [49 μm × 14.5 μm] of an ECD sample prior to calcination obtained by XRF-CT. The thickness of the hydrotalcite layer represented by its nickel content is 1.2 ± 0.2 μm. Reprinted with permission from Basile et al. Adv. Funct. Mater. 20 (2010) 4117–4126. Copyright 2010 Wiley-VCH.

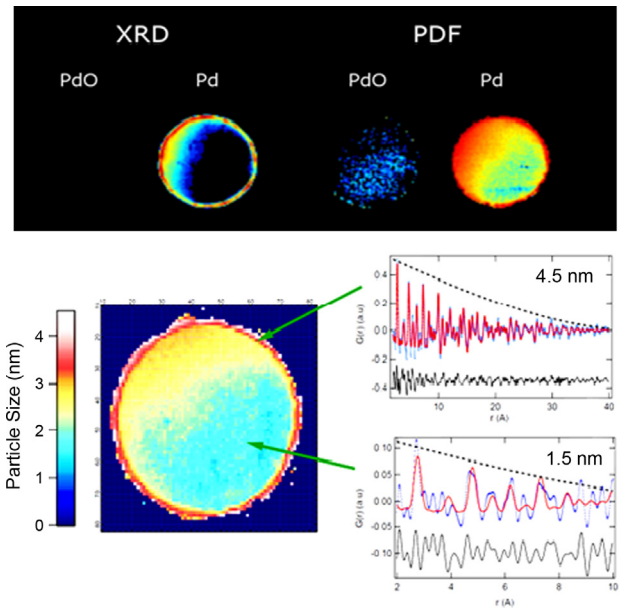

Fig. 10. (Top) Comparison of information from XRD-CT (left) and PDF-CT (right) after sample reduction. (Bottom) Distribution of particle sizes of fcc Pd within the catalyst body under reducing conditions. (Bottom Right) portions of the PDF data for selected pixels at the edge and interior of the catalyst body. Reprinted with permission from Jacques et al. Nat. Commun. 4 (2013) 2536. Copyright 2013 Nature Publishing Group.

dispersed Cr and Fe although with Y localised in spots. However the μ-XRF also revealed that in some cases the active (Ni) coverage was not uniform for both ECD samples. μ-XRD tomography data showed that regions containing large amounts of 'active' comprised of predominantly NiO in addition to α-Al_2O_3 and $NiAl_2O_4$; the source of this excess NiO was thought to be due to an excessive build-up of the hydrotalcite precursor. Analysis of the XRD peak full widths yielded an average active coating thickness of 2 μm; this was also confirmed by μ-XRF tomography data as shown in Fig. 9c. In contrast, the conventionally prepared sample contained on average a thicker coating of active although this was somewhat more uneven; some large zones with no coating were observed next to areas with thicker coating. More α-Al_2O_3 was also found on the sample which was thought to be due to the application of an additional boehmite wash although it was not possible to rule out that oxidation of the foam had also taken place. However, unlike the ECD samples, the NiO and $NiAl_2O_4$ distributions were very similar and much more uniform therefore showed the same molar ratios on the microscale as in the bulk. Furthermore the washcoat had also ingressed into the inner part of the foam. Thus overall it was concluded that the catalysts prepared by ECD were formed by the phases expected from the decomposition of HT compounds.

The catalysts were then compared in performance for methane activation. It was observed that whilst one of the ECD samples deactivated gradually with time-on-stream, the other showed a good and stable performance with a performance to rival that of a commercial catalyst, despite its lower nickel loading. It was proposed by μ-XRD-CT that the cause of deactivation for one of the ECD samples was the loss of the coating during reaction; the resultant exposed parts lead to carbon deposition over the uncovered support, or partial sintering of the catalyst. On the other hand, the steady-state performance of the other ECD sample pointed towards a good stability/adhesion/uniformity of the catalytic layer. It should be noted however that in the active ECD sample that both the fcc Ni phase and the alumina-containing layers appeared to be more intermixed after reaction suggesting that the severe reaction conditions (hydrothermal conditions and high temperature) cause migration of Al from the metallic foam into the catalyst washcoat and nickel diffusion into the alumina takes place.

3.1.6. *Pair distribution function computed tomography*

A potential Achilles heel of the XRD-CT technique is the inability to characterise phases/materials not possessing long range order, particularly then amorphous and nano-scale materials. However the emergence in recent times of the X-ray pair distribution function (PDF) method as a technique capable of obtaining reliable, quantitative information regarding nanostructure offers a way forward [53]. In a recent study by Jacques et al. the successful coupling of pair distribution function (PDF) analysis with computed tomography (CT) to yield the first data obtained by the new technique of PDF-CT was demonstrated, allowing for the physicochemical profiling of the nano-properties of materials and their distribution in three-dimensional space at the micron scale [53]. In many cases the nature of the (shortest chemical bond) is sufficient to distinguish between the components rendering the technique capable of providing chemical bond or chemical species contrast tomography irrespective of kinetic state.

In this demonstration the distribution of Pd species which comprise the active component for both hydrogenation and oxidation reactions was studied [92,93]. Fig. 10 (left) shows the reconstructed distributions of selected atomic scattering pairs pertaining to the same crystalline phases e.g. the components with peaks at 3.44 and 2.71 Å in the radial distribution functions due to Pd-Pd pairs in PdO and fcc Pd, respectively. In the treated sample, the XRD-CT map in Fig. 10 suggests a preferential distribution of both PdO and Pd phases at the sample periphery. Critically PDF-CT not only confirms the preferential concentration of the Pd/PdO but it also reveals a number of 'diffraction silent' metallic Pd particles beyond the sample periphery and on the inside of the catalyst body. The observation that the diffraction silent PDF-CT signal in the core of the catalyst is from small nanoparticles is verified by further quantitative analysis of representative PDFs from voxels from the periphery and the core shown in Fig. 10 (right). A direct inspection clearly reveals that the PDF signal is diminishing more quickly in the latter case suggesting that the diffraction silent nanoparticles in the centre of the catalyst body must be very small. Using a spherical model as an approximation of the particles present to the calculated PDF, a good fit for

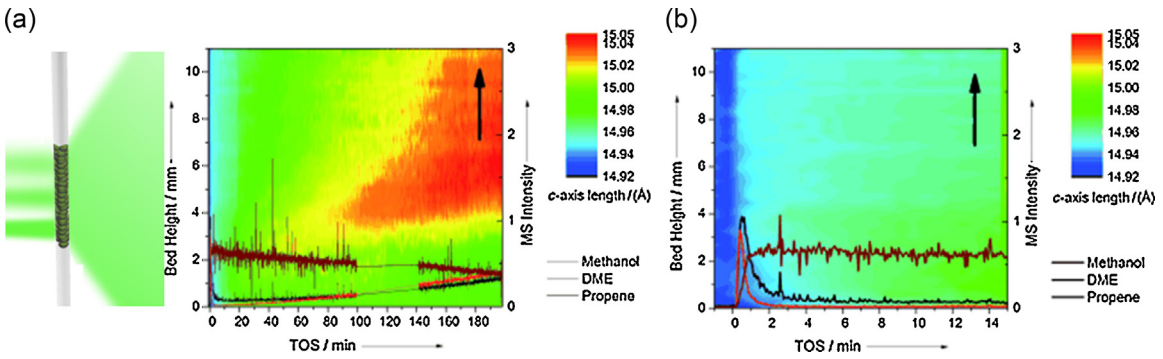

Fig. 11. (Left) Schematic illustrating how multiple XRD measurements are performed down the length of a reactor tube. In (a) are shown the changes in the *c*-axis derived from a detailed analysis of the SAPO-34 (4% silicon) structure during MTO (30 mL/min flow). The direction of reactant flow is indicated by the large black arrows. Plot (b) represents an enlargement of the first 15 min of plot (a). The lines at the bottom of both plots correspond to the signals recorded on the mass spectrometer (MS) for the methanol reactant and products (dimtheyl ether(DME) and propene) measured at the reactor outlet. Reprinted with permission from Wragg et al. Angew. Chem. Int. Ed. 51 (2012) 7956–7959. Copyright 2012 Wiley-VCH.

a nanoparticle diameter of ~1.4 nm was obtained. In contrast the particles located at the sample periphery exceed ~4 nm.

3.2. Catalytic reaction

3.2.1. Z-scan method

Packed bed reactors form the basis of numerous industrial catalysis studies. For the most part they are mounted horizontally but in a study by O'Brien et al. a vertically mounted catalyst bed was used to examine the problem of molybdenum volatilisation from methanol selective oxidation catalysts [29]. Up until this study there had been some debate in the literature as to, whether volatile Mo-methanol species were responsible or else water played a role leading to deactivation. Thus methanol and water were fed separately in the gas stream onto a packed bed within a large 5 mm i.d. capillary reactor (chosen to improve sampling statistics as well as to work under more plug-flow like conditions). In order to determine whether Mo volatilisation occurred from MoO_3 at reaction temperature more readily in a methanol or water atmosphere, transmission XRD data, the inelastic and fluorescence signals, UV–vis and Raman data were recorded at the same time down the length of the reactor bed (~1.1 cm) as a function of time. Since Methanol is a reductant, MoO_3 was shown by all techniques to reduce to form MoO_2, although this was via the intermediate phases $Mo_xO_yC_z$ and MoO_xH_y. The rate at which MoO_2 formed varied down the length of the bed with the outlet of the reactor containing more of the phase than the inlet. Little evidence for Mo volatilisation could be seen from the diffraction data whilst the sample was too dark to obtain a reliable spectroscopic signal however, on closer inspection of the inelastic scattering/fluorescence data, clear evidence could be seen of a loss of Mo due to an increase in the measured inelastic signal at the top of the reactor bed. It was proposed that this was caused by a density decrease so could not be due to the formation of more MoO_2, since this is denser than the MoO_3, $Mo_xO_yC_z$ and MoO_xH_y phases and therefore in all likelihood, was due to Mo loss. It was not possible to tell which of the observed phases was primarily associated with Mo volatisation. In contrast, no such changes were observed during treatment in water or during similar experiments performed on the Fe_2MoO_4 phase (the principle component of methanol selective oxidation catalysts) [13].

The same approach and setup was employed by Wragg et al. to look at SAPO-34 during the methanol-to-olefin (MTO) reaction – this study serving as a follow-up to some single point measurements where anisotropic changes in the unit-cell dimensions were shown to be related to the build-up of intermediate species in the cages of the SAPO-34 framework and eventually to catalyst deactivation [42,43,94]. In this particular study a huge variation of lattice parameter across the reactor bed was seen (predominantly in the c-axis direction) – see Fig. 11. The cause of this c-axis expansion was shown (using online MS) to correlate with the beginning of propene production (and accompanying decline of methanol and dimethyl ether (DME) flow-through) to be due to the formation of hydrocarbon pool (HCP) species which was confirmed by kinetic modelling [42]. This *c*-axis expansion in the catalyst was first observed towards the end of the catalyst bed and to progress up the bed against the reactant flow over a period of 6 min. The formation of heavy polyaromatic coke species lead to yet further expansion of the unit cell however this time the expansion begun at the front of the bed expanding towards the bed end. Importantly the same observations were made using a higher methanol feed rate (50 mL/min) although a smaller *c*-axis expansion is observed, suggesting less HCP species formation with shorter contact times. The observation of HCP species formation is consistent with an autocatalytic reaction scheme and that methanol is directly involved in the continued formation of heavy coke during the MTO.

3.2.2. Single particle study

A combination of both μ-XRD-CT and X-ray absorption μ-CT (see Fig. 12) has previously been used to study the solid state changes in mm-sized $Ni/\gamma\text{-}Al_2O_3$ catalyst bodies in 2D and 3D after impregnation, during N_2 calcination, calcination in air, H_2 reduction and finally during the CO methanation reaction [48]. During each treatment/reaction stage the same 2D cross section was profiled as a function of temperature/time so as to be able to examine what effects (if any) the treatment conditions had on the nature and spatial distribution of the species present in the sample. Furthermore by performing a combined study it was also possible to verify that the μ-XRD-CT results were not (too) diffraction biased i.e. that there was not large amounts of diffraction-silent material located elsewhere in the catalyst particle. As with much of the previous study on $[Ni(en)(H_2O)_4]Cl_2/\gamma\text{-}Al_2O_3$ little change in Ni distribution was observed during calcination and reduction in H_2 although a 60% increase in Bragg scattering of the metallic Ni observed after H_2 treatment suggested that after calcination a significant portion of the Ni species are not crystalline enough to observe with XRD-CT. Furthermore the 60% increase seen in the XRD signal occurred during the exothermic oxidation step. Interestingly the fact that no large scale migration of Ni was observed during the pre-treatment stages clearly demonstrates the importance of the impregnation step for determining the distribution of the active component.

The subsequent methanation reaction was performed during temperature ramping from 200 to 450 °C with catalytic activity observed as the temperature approached 340 °C; the 2D XRD-CT

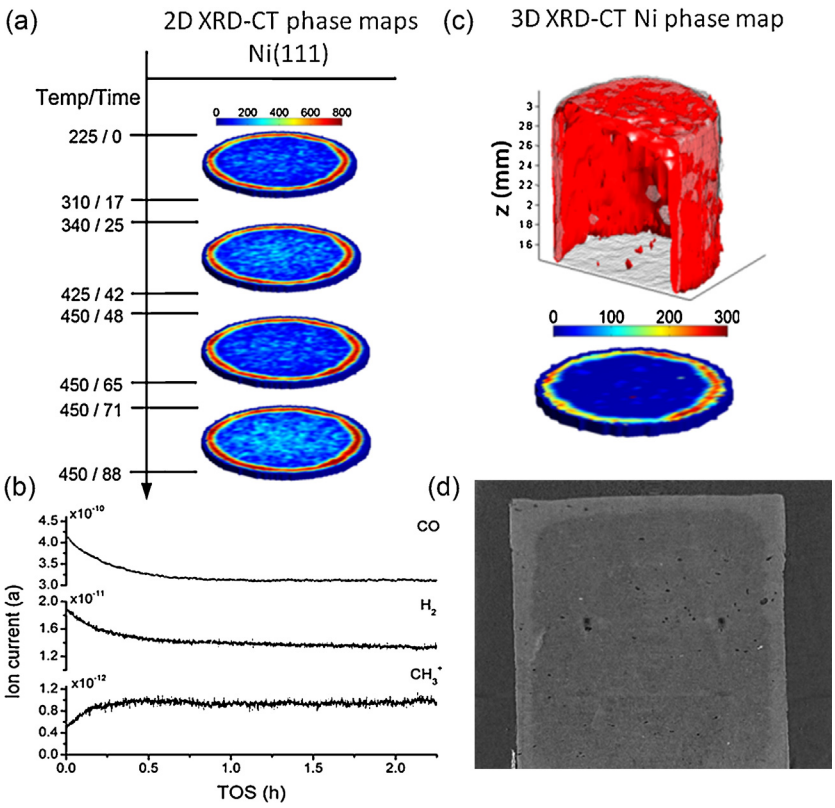

Fig. 12. The catalytic methanation over Ni catalyst measured in situ initially with 2D diffraction tomography during heat ramping and then with 3D diffraction tomography ('stitched' 2D scans). During the catalytic process there was very little change in both the crystalline and non-crystalline distributions and, as indicated by the high quality summed 1D images, no in situ reaction intermediates where observed. The catalytic methanation over the prepared Ni catalyst measured in situ initially with 2D μ-XRD-CT during heat ramping and then with 3D μ-XRD-CT ('stitched' 2D scans). The catalytic reaction was followed by in situ mass spectrometry. During the catalytic process there was very little change in both the crystalline and non-crystalline distributions and, as indicated by the high quality summed 1D XRD patterns, no in situ reaction intermediates where observed. Reproduced from O'Brien et al. Chem. Sci. 3 (2012) 509-523 with permission from The Royal Society of Chemistry

data demonstrating fcc Ni to be the only crystalline phase present on the sample and therefore the active phase. Furthermore no significant change in Ni particle size was observed whilst the X-ray absorption μ-CT confirmed that no migration of Ni occurred during reaction. Again 3D XRD-CT data demonstrated that the observations made from the 2D cross-section where representative of the sample in its entirety.

3.3. Catalyst deactivation

3.3.1. Heavy metal poisoning

Poisoning or fouling of a catalyst is a common mode of deactivation which it is not well understood. Catalysts can deactivate temporarily (site blocking) or permanently (structural alteration) [95–97]. Heavy metal deposition usually leads to the latter and is becoming an increasingly pertinent issue as society requires that processes operate more efficiently and with more sustainable feedstocks. Using a similar approach to Basile et al. μ-XRF imaging combined with μ-X-ray Absorption Near Edge Spectroscopy (μ-XANES) and μ-XRD-CT were used to investigate metal poisoning of Fluid Catalytic Cracking (FCC) zeolite catalysts by Ni and V [91,98]. Neither Ni nor V are present in the initial catalyst but are typically present in crude oil and cause damage to the active zeolite phase. The 3D XRF maps (Fig. 13) show an uneven distribution of these metals after reaction in an industrial cracking unit. An eggshell of Ni with 10–15 μm thickness (Fig. 13a) was observed and a more even distribution across the particle but still egg-shell type distribution of V was observed (Fig. 12b). XANES show the Ni is Ni^{2+} either $NiAl_2O_4$ or NiO species, and the V is V^{4+} and V^{5+} of V_2O_4 and V_2O_5 [98]. Individual patterns from μ-XRD-CT from the middle of the sample fresh and reacted samples were summed using 2700 XRD patterns per sample allowing the detection of even minimal phases. The fresh sample contains zeolite Y, kaolinite, boehmite and anatase (from TiO_2 impurities in kaolinite clay) and with the exception of amorphous silica this is all the catalyst components. After reaction the XRD is very different with a decrease in zeolite Y phase due to a loss in crystallinity, a mullet phase appears due to a series of phase transitions of the kaolinite and the boehmite dehydrates and forms γ-Al_2O_3. For zeolite Y a random distribution in the fresh catalyst is observed which becomes an egg-yolk distribution in the deactivated sample (Fig. 13e). The zeolite at the periphery of the particle undergoes dealumination and experiences a loss of Brønsted acidity. This compares well to the egg-shell distribution of the poisons. 2D Si/Al ratio maps show that dealumination of the catalyst particle on the fresh and post-reaction, with the Si/Al ratio ranging from 60 at the periphery to ~ 25 at the interior for the post-reaction sample. The authors suggested that the Ni and V in combination with high boiling point hydrocarbons are unable to access the centre of the particle and so significantly higher coke formation at the periphery is observed. During regeneration coke combustion creates localised hot spots which have a greater impact on zeolite destruction and related dealumination.

3.4. Beyond catalytic materials

3.4.1. Cement hydration

Cement chemistry has long been studied but still many issues unresolved in terms of linking the cement properties with the evolving chemistry. A number of recent XRD-CT experiments on cement microstructure have been performed that, for the most

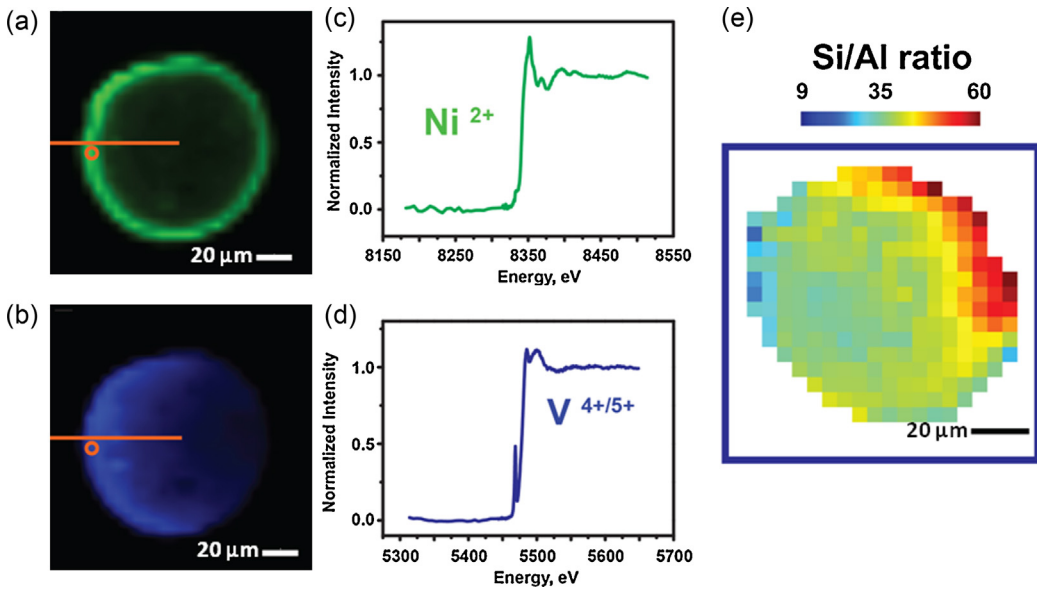

Fig. 13. µ-XRF 2D chemical maps of Ni (a) and V (b) for a used FCC catalyst particle. The orange lines illustrate the position where the intensity profiles were taken. (c) Ni and (d) V K-edge XANES spectra recorded from the orange circle for the particle. e) 2D reconstruction of the zeolite Si/Al ratio for particle; the thermal scale bar corresponds to the calculated zeolite Si/Al ratio for the particle. Reprinted with permission from Ruiz-Martinez et al. Angew. Chem. Int. Ed. 52 (2013) 5983–5987. Copyright 2013 Wiley-VCH.

part, have tried to benchmark the method [46,99,100]. Actual time-resolved XRD-CT data examining cement hydration in situ to monitor the evolution of the sample microstructure at different hydration stages has recently been reported by Voltolini et al. [100] Since hydration is a relatively fast process the authors used a cold air stream to lower the temperature (289.2 K) to slow down the kinetics during data collection (2 h). An example of the data recorded in this experiment are given in Fig. 14 and take the form of the original phase maps before and after 2 h as well as a difference map. These phase composition maps were generated from a Rietveld analysis of the XRD data furthermore required since the calcium silicate hydrate (CSH) phase is diffraction amorphous and required determination using a mass balance procedure. The number of uniquely identifiable phases present is impressive and testament to the power of chemical/diffraction imaging, however the very long collection times employed leads to the appearance of artefacts in the data (very faint 'waves'/lines seen in the distribution maps) as phases such as calcium silicate hydrate (CSH) and ettringite appear and disappear. Furthermore the study was able to differentiate between particles based on size i.e. between larger grains and the powder particles of ettringite – in a way this type of information could be considered a 6th dimension (a measurement 'dimension') to the information available. However these multiphase maps clearly showed that hydrate phases surround the

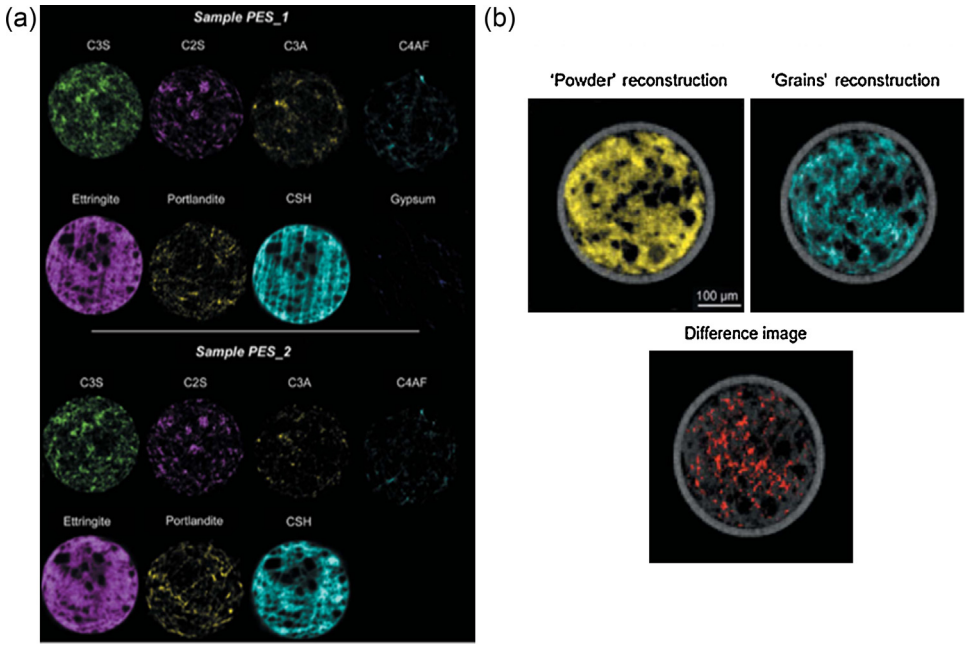

Fig. 14. Distribution of the phases present in the sample, at two different times during the hydration reaction [acceleration (PES_1) and deceleration (PES_2) periods]. (a) The distribution maps of all clinker and hydration phases displayed for each experiment. (b) Distribution of ettringite 'crystallinity' (left) spatial distribution maps of the finer and (right) coarser ettringite crystals are plotted. The difference image highlights where the largest ettringite grains are located. Reproduced from Voltolini et al. J. Appl. Cryst. 46 (2013) 142–152 doi:10.1107/S0021889812046985 with permission from the International Union of Crystallography.

un-hydrated clinker phases, with no overlap, whilst the global difference map shows the locations where clinker dissolution and hydrate precipitation occurred. Furthermore it was also possible to observe a higher rate of precipitation in the region close to the capillary wall and a slightly faster dissolution of some clinker granules, richer in CSH. The study also demonstrated the importance of the spatial distribution of CSH and in particular how it fills the areas around the clinker phases and voids a result that has implications in terms of the mechanical properties of cement-based material.

3.5. Potential experiments

An obvious place to start when discussing potential future μ-XRD-CT measurements would be previous X-ray absorption μ-CT experiments where more chemical information is useful or even desired. In principle any sample where microstructure changes have an important impact on the performance of devices a few mm to cm in size will surely benefit from a more detailed understanding of the chemistry at play. For example and only example, battery research where μ-XRD-CT might enable for a more conclusive or even inclusive characterisation of polysulphide layers on lithium sulphide battery cathodes during charge/discharge or else to better understand the chemical processes that give rise to effects such as sintering or coarsening often seen in solid oxide fuel cells (SOFCs) [101,102]. Alloy formation and dendrite growth under process conditions might also benefit from being able to identify phase (particularly polymorphs) particularly during the common problem of phase segregation [103]. Beyond materials science there may well also be possibilities in medical imaging for example investigating the growth of artificial and natural 3D tissue structures in bone, or teeth or for medical screening purposes [49,104–106].

3.6. Conclusions and outlook

XRD-CT methods using micro-beams are becoming more routinely applied across 3rd generation synchrotrons since the first demonstration by Bleuet et al. with to date capacity demonstrated at the European Synchrotron Radiation Facility (ESRF), Diamond Light Source and the Advanced Photon Source (APS) [23,98,107,108]. In many ways the examples given in this study coupled with the expected further developments in source/detector technology and data handling, force us to contemplate whether such methods might soon become the goto technology to ensure a more comprehensive examination of materials properties. Add to this the developments in sample environment where for example it is now possible to perform imaging measurements at the correct temperatures and pressures [109]. Furthermore the techniques now offer the possibility for obtaining reciprocal and real space information from the same part of the sample using beams approaching sub-micron in size with an acquisition rate at ~25 Hz or greater [53]. As such there has never been a better time for industrial research to obtain unprecedented insight into the behaviour of samples under highly relevant process conditions for the determination/extraction of those all-too-crucial structure-activity relationships from samples in the solid-state. The quality (here we mean better spatial and time resolution as well as data with better signal-to-noise statistics) of the 5 dimensional information will only improve with the advent of more intense sources (i.e. upgraded 3rd generation and 4th generation sources) as well as better performing detectors and the development of post-processing capabilities (software) [110]. Ultimately the improvement in these parameters will enable the fast acquisition of chemical imaging data using nanobeams allowing for the observation of individual nanoparticles under process conditions. Indeed facilities for performing such studies already exist [111,112]. A potential drawback for the application of nanobeams is that XRD-CT relies on their being a number of particles in a voxel that satisfy the Bragg condition and as this number diminishes so the data will become more susceptible to both preferred orientation and single crystal diffraction 'effects'. However as has been previously shown (Section 3.4.1) there are ways to mitigate this problem although a new processing strategy will be required for reconstructing what would effectively be single crystal diffraction tomography data. It should also be mentioned that the radiation dose from nanobeams needs to be carefully considered/managed.

It is not to say that more traditional methods (in situ XRD and XAFS) have no value since such methods provide for a more detailed characterisation of the material under investigation i.e. for identification of new structures/physical properties in terms of their activity although care must be taken that the sample under investigation does not exhibit some axial variation. Combining techniques (including X-ray and optical spectroscopic measurements) has also become more commonplace allowing users to almost 'pick' their technique combination to suit the reaction they are following [113,114].

The development of lab-based X-ray sources is also worth noting although here the most likely viable option is through the application of white beam imaging techniques since imaging in real time requires a certain amount of brute force (X-ray flux) which is not always possible with monochromatic sources [61,63]. One has to consider however how best to implement such setups since the X-ray intensity still requires a containment hutch similar to that used in a synchrotron. An alternative that one cannot ignore is the development of tabletop synchrotrons which offer the possibility of a compact bright source of ultrafast synchrotron radiation with appreciable degree of spatial coherence [115]. Furthermore they are not limited to producing X-rays. However, these should still be considered as work in progress requiring that a certain set of problems be overcome before these become readily practicable [116].

As previously indicated the future of XRD-imaging methods however need not remain the preserve of materials science. The generation of chemical signals in space allows for less ambiguous diagnosis than that offered by X-ray contrast and one can imagine that with the continued technological advancements, particularly in detector technology, that chemical imaging methods will eventually become the norm in medical, archaeological, palaeontology and cultural heritage.

It has been 100 years since Max von Laue was awarded the Nobel prize in physics for the 'discovery of the diffraction of X-rays by crystals' and it seems that the coming years will see the application of this discovery broaden into areas that were, until recently, not considered [117].

Acknowledgements

The authors would like to acknowledge the contributions of Profs. Paul Barnes, Robert J. Cernik, Bert M. Weckhuysen and Dr. Matthew G. O'Brien towards the development of Diffraction Imaging, to the synchrotron light sources (particularly ESRF) for access to the facilities and to financial support from EPSRC (UK) and NWO (NL).

References

[1] G. Ertl, Angew. Chem. Int. Ed. 47 (2008) 3524–3535.
[2] M. Bowker, P. Stone, R. Bennett, N. Perkins, Surf. Sci. 511 (2002) 435–448.
[3] D.W. Goodman, J. Catal. 216 (2003) 213–222.
[4] F. Gao, D.W. Goodman, Annu. Rev. Phys. Chem. Vol63 (63) (2012) 265–286.
[5] G.A. Somorjai, Surf. Sci. 299 (1994) 849–866.
[6] H.J. Freund, H. Kuhlenbeck, J. Libuda, G. Rupprechter, M. Baumer, H. Hamann, Top. Catal. 15 (2001) 201–209.

[7] M. Bron, D. Teschner, A. Knop-Gericke, B. Steinhauer, A. Scheybal, M. Havecker, D. Wang, R. Fodisch, D. Honicke, A. Wootsch, R. Schlogl, P. Claus, J. Catal. 234 (2005) 37–47.
[8] M. Baerns, R. Imbihl, V.A. Kondratenko, R. Kraehnert, W.K. Offermans, R.A. van Santen, A. Scheibe, J. Catal. 232 (2005) 226–238.
[9] H. Oosterbeek, Phys. Chem. Chem. Phys. 9 (2007) 3570–3576.
[10] K. Roy, C.P. Vinod, C.S. Gopinath, J. Phys. Chem. C 117 (2013) 4717–4726.
[11] B.M. Weckhuysen, Phys. Chem. Chem. Phys. 5 (2003) 4351–4360.
[12] M.A. Banares, I.E. Wachs, J. Raman Spectrosc. 33 (2002) 359–380.
[13] M.G. O'Brien, A.M. Beale, S.D.M. Jacques, M. Di Michiel, B.M. Weckhuysen, Appl. Catal. A: Gen. 391 (2011) 468–476.
[14] A. Rochet, V. Moizan, F. Diehl, C. Pichon, V. Briois, Catal. Today 205 (2013) 94–100.
[15] E. Kleymenov, J. Sa, J. Abu-Dahrieh, D. Rooney, J.A. Van Bokhoven, E. Trous-sard, J. Szlachetko, O.V. Safonova, M. Nachtegaal, Catal. Sci. Technol. 2 (2012) 373–378.
[16] K.H. Cats, I.D. Gonzalez-Jimenez, Y. Liu, J. Nelson, D. van Campen, F. Meirer, A.M.J. van der Eerden, F.M.F. de Groot, J.C. Andrews, B.M. Weckhuysen, Chem. Commun. 49 (2013) 4622–4624.
[17] H. Karaca, J. Hong, P. Fongarland, P. Roussel, A. Griboval-Constant, M. Lacroix, K. Hortmann, O.V. Safonova, A.Y. Khodakov, Chem. Commun. 46 (2010) 788–790.
[18] B.M. Weckhuysen, Angew. Chem. Int. Ed. 48 (2009) 4910–4943.
[19] A.M. Beale, S.D.M. Jacques, B.M. Weckhuysen, Chem. Soc. Rev. 39 (2010) 4656–4672.
[20] J.D. Grunwaldt, C.G. Schroer, Chem. Soc. Rev. 39 (2010) 4741–4753.
[21] J.-D. Grunwaldt, B. Kimmerle, A. Baiker, P. Boye, C.G. Schroer, P. Glatzel, C.N. Borca, F. Beckmann, Catal. Today 145 (2009) 267–278.
[22] I.L.C. Buurmans, B.M. Weckhuysen, Nat. Chem. 4 (2012) 873–886.
[23] P. Bleuet, E. Welcomme, E. Dooryhee, J. Susini, J.L. Hodeau, P. Walter, Nat. Mater. 7 (2008) 468–472.
[24] M. Alvarez-Murga, P. Bleuet, J.L. Hodeau, J. Appl. Crystallogr. 45 (2012) 1109–1124.
[25] A.M. Beale, J. Ruiz-Martinez, B.M. Weckhuysen, In-Situ Characterization of Heterogeneous Catalysts, Wiley-VCH Verlag GmbH & Co. KGaA, 2013, pp. 441–473.
[26] M. Dierolf, A. Menzel, P. Thibault, P. Schneider, C.M. Kewish, R. Wepf, O. Bunk, F. Pfeiffer, Nature 467 (2010) 436–482.
[27] P. Thibault, M. Dierolf, A. Menzel, O. Bunk, C. David, F. Pfeiffer, Science 321 (2008) 379–382.
[28] M.G. O'Brien, A.M. Beale, S.D.M. Jacques, T. Buslaps, V. Honkimaki, B.M. Weck-huysen, J. Phys. Chem. C 113 (2009) 4890–4897.
[29] M.G. O'Brien, A.M. Beale, S.D.M. Jacques, M. Di Michiel, B.M. Weckhuysen, Chemcatchem 1 (2009) 99–102.
[30] G. Harding, J. Kosanetzky, U. Neitzel, Med. Phys. 14 (1987) 515–525.
[31] G. Harding, J. Kosanetzky, Nucl. Instrum. Methods Phys. Res. Sect. A 280 (1989) 517–528.
[32] G. Harding, M. Newton, J. Kosanetzky, Phys. Med. Biol. 35 (1990) 33–41.
[33] C. Hall, P. Barnes, J.K. Cockcroft, S.D.M. Jacques, A.C. Jupe, X. Turrillas, M. Hanfland, D. Hausermann, Anal. Commun. 33 (1996) 245–248.
[34] S.D.M. Jacques, K. Pile, P. Barnes, Cryst. Growth Des. 5 (2005) 395–397.
[35] A.M. Beale, S.D.M. Jacques, J.A. Bergwerff, P. Barnes, B.M. Weckhuysen, Angew. Chem. Int. Ed. 46 (2007) 8832–8835.
[36] R.J. Cernik, C.C.T. Hansson, C.M. Martin, M. Preuss, M. Attallah, A.M. Korsun-sky, J.P. Belnoue, T.S. Jun, P. Barnes, S. Jacques, T. Sochi, O. Lazzari, J. Appl. Crystallogr. 44 (2011) 150–157.
[37] O. Lazzari, S. Jacques, T. Sochi, P. Barnes, Analyst 134 (2009) 1802–1807.
[38] O. Lazzari, C.K. Egan, S.D.M. Jacques, T. Sochi, M. Di Michiel, R.J. Cernik, P. Barnes, J. Synchrotron Radiat. 19 (2012) 471–477.
[39] P. Barnes, A.C. Jupe, S.D.M. Jacques, S.L. Colston, J.K. Cockcroft, D. Hooper, M. Betson, S. Bare, A.R. Rennie, J. Shannahan, M.A. Carter, W.D. Hoff, M.A. Wilson, M.C. Phillipson, Nondestructive Test. Eval. 17 (2001) 143–167.
[40] L. Espinosa-Alonso, M.G. O'Brien, S.D.M. Jacques, A.M. Beale, K.P. de Jong, P. Barnes, B.M. Weckhuysen, J. Am. Chem. Soc. 131 (2009) 16932–16938.
[41] V. Middelkoop, P. Boldrin, M. Peel, T. Buslaps, P. Barnes, J.A. Darr, S.D.M. Jacques, Chem. Mater. 21 (2009) 2430–2435.
[42] D.S. Wragg, M.G.O. Brien, F.L. Bleken, M. Di Michiel, U. Olsbye, H. Fjellvag, Angew. Chem. Int. Ed. 51 (2012) 7956–7959.
[43] D.S. Wragg, F.L. Bleken, M.G. O'Brien, M. Di Michiel, H. Fjellvag, U. Olsbye, Phys. Chem. Chem. Phys. 15 (2013) 8662–8671.
[44] M. Alvarez-Murga, P. Bleuet, L. Marques, C. Lepoittevin, N. Boudet, G. Gabarino, M. Mezouar, J.L. Hodeau, J. Appl. Crystallogr. 44 (2011) 163–171.
[45] M. Alvarez-Murga, P. Bleuet, G. Garbarino, A. Salamat, M. Mezouar, J.L. Hodeau, Phys. Rev. Lett. 109 (2012) 025502.
[46] G. Artioli, T. Cerulli, G. Cruciani, M.C. Dalconi, G. Ferrari, M. Parisatto, A. Rack, R. Tucoulou, Anal. Bioanal. Chem. 397 (2010) 2131–2136.
[47] S.D.M. Jacques, M. Di Michiel, A.M. Beale, T. Sochi, M.G. O'Brien, L. Espinosa-Alonso, B.M. Weckhuysen, P. Barnes, Angew. Chem. Int. Ed. 50 (2011) 10148–10152.
[48] M.G. O'Brien, S.D.M. Jacques, M. Di Michiel, P. Barnes, B.M. Weckhuysen, A.M. Beale, Chem. Sci. 3 (2012) 509–523.
[49] C.K. Egan, S.D.M. Jacques, M. Di Michiel, B. Cai, M.W. Zandbergen, P.D. Lee, A.M. Beale, R.J. Cernik, Acta Biomater. 9 (2013) 8337–8345.
[50] W. De Nolf, K. Janssens, Surf. Interface Anal. 42 (2010) 411–418.
[51] http://www.datasqueezesoftware.com/
[52] S.J.L. Billinge, I. Levin, Science 316 (2007) 561–565.
[53] S.D.M. Jacques, M. Di Michiel, S.A.J. Kimber, X. Yang, R.J. Cernik, A.M. Beale, S.J.L. Billinge, Nat. Commun. 4 (2013) 2536.
[54] S.L. Colston, P. Barnes, A.C. Jupe, S.D.M. Jacques, C. Hall, P. Livesey, J. Dransfield, N. Meller, G.C. Maitland, Cem. Concr. Res. 35 (2005) 2223–2232.
[55] B. Buras, J.S. Olsen, L. Gerward, Nucl. Instrum. Methods 135 (1976) 193–195.
[56] M.G. Bisogni, M. Campbell, M. Conti, P. Delogu, M.E. Fantacci, E.H.M. Heijne, P. Maestro, G. Magistrati, V.M. Marzulli, G. Meddeler, B. Mikulec, E. Pernigotti, V. Rosso, C. Schwarz, W. Snoeys, S. Stumbo, J. Watt, Conference on EUV, X-Ray, and Gamma-Ray Instrumentation for Astronomy IX, San Diego, Ca, 1998, pp. 298–304.
[57] S.R. Amendolia, M.G. Bisogni, U. Bottigli, A. Ceccopieri, P. Delogu, G. Dipasquale, M.E. Fantacci, P. Maestro, A. Marchi, P. Oliva, R. Palmiero, E. Pernigotti, V. Rosso, A. Stefanini, S. Stumbo, Nucl. Instrum. Methods Phys. Res. Sect. A 461 (2001) 422–424.
[58] R. Ballabriga, M. Campbell, E. Heijne, X. Llopart, L. Tlustos, W. Wong, Nucl. Instrum. Methods Phys. Res. Sect. A 633 (2011) S15–S18.
[59] I. Ordavo, S. Ihle, V. Arkadiev, O. Scharf, H. Soltau, A. Bjeoumikhov, S. Bjeoumikhova, G. Buzanich, R. Gubzhokov, A. Guenther, R. Hartmann, P. Holl, N. Kimmel, M. Kuehbacher, M. Lang, N. Langhoff, A. Liebel, M. Radtke, U. Rein-holz, H. Riesemeier, G. Schaller, F. Schopper, L. Strueder, C. Thamm, R. Wedell, Nucl. Instrum. Methods Phys. Res. Sect. A 654 (2011) 250–257.
[60] O. Scharf, S. Ihle, I. Ordavo, V. Arkadiev, A. Bjeoumikhov, S. Bjeoumikhova, G. Buzanich, R. Gubzhokov, A. Guenther, R. Hartmann, M. Kuehbacher, M. Lang, N. Langhoff, A. Liebel, M. Radtke, U. Reinholz, H. Riesemeier, H. Soltau, L. Strueder, A.F. Thuenemann, R. Wedell, Anal. Chem. 83 (2011) 2532–2538.
[61] R.J. Cernik, K.H. Khor, C. Hansson, J. R. Soc. Interface 5 (2008) 477–481.
[62] M.D. Wilson, S.J. Bell, R.J. Cernik, C. Christodoulou, C.K. Egan, D. O'Flynn, S. Jacques, S. Pani, J. Scuffham, P. Seller, P.J. Sellin, R. Speller, M.C. Veale, IEEE Trans. Nucl. Sci. 60 (2013) 1197–1200.
[63] S.D.M. Jacques, C.K. Egan, M.D. Wilson, M.C. Veale, P. Seller, R.J. Cernik, Analyst 138 (2013) 755–759.
[64] J. Scuffham, M.C. Veale, M.D. Wilson, P. Seller, J. Instrum. 8 (2013) (Article No. P10024).
[65] J.A. Greenberg, M. Hassan, K. Krishnamurthy, D. Brady, Analyst 139 (2014) 709–713.
[66] K.P. MacCabe, A.D. Holmgren, M.P. Tornai, D.J. Brady, Appl. Opt. 52 (2013) 4582–4589.
[67] P. Llull, X. Liao, X. Yuan, J. Yang, D. Kittle, L. Carin, G. Sapiro, D.J. Brady, Opt. Express 21 (2013) 10526–10545.
[68] U. Bonse, M. Hart, Appl. Phys. Lett. 6 (1965) 155.
[69] T.J. Davis, D. Gao, T.E. Gureyev, A.W. Stevenson, S.W. Wilkins, Nature 373 (1995) 595–598.
[70] D. Guersoy, M. Das, in: A. Inc, C.C.O. Univ. Cent. Florida, D.Q.E. Photon, I. Inc., P. Medtronic Inc. (Eds.), Conference on Medical Imaging – Physics of Medical Imaging, Lake Buena Vista, FL, 2013.
[71] J. Kaspar, P. Fornasiero, M. Graziani, Catal. Today 50 (1999) 285–298.
[72] E. Aneggi, M. Boaro, C. de Leitenburg, G. Dolcetti, A. Trovarelli, J. Alloys Compd. 408 (2006) 1096–1102.
[73] C. Slostowski, S. Marre, J.-M. Bassat, C. Aymonier, J. Supercrit. Fluids 84 (2013) 89–97.
[74] N. Singhania, E.A. Anumol, N. Ravishankar, G. Madras, Dalton Trans. 42 (2013) 15343–15354.
[75] P. Boldrin, A.K. Hebb, A.A. Chaudhry, L. Otley, B. Thiebaut, P. Bishop, J.A. Darr, Ind. Eng. Chem. Res. 46 (2007) 4830–4838.
[76] V. Middelkoop, C.J. Tighe, S. Kellici, R.I. Gruar, J.M. Perkins, S.D.M. Jacques, P. Barnes, J.A. Darr, J. Supercrit. Fluids 87 (2014) 118–128.
[77] M. Chen, C.Y. Ma, T. Mahmud, J.A. Darr, X.Z. Wang, J. Supercrit. Fluids 59 (2011) 131–139.
[78] V. Middelkoop, S.D.M. Jacques, M.G. O'Brien, A.M. Beale, P. Barnes, J. Mater. Sci. 43 (2008) 2222–2228.
[79] J.R. Regalbuto, Catalyst Preparation: Science and Engineering, CRC Press, Boca Raton, 2006.
[80] S. Mitchell, N.-L. Michels, J. Perez-Ramirez, Chem. Soc. Rev. 42 (2013) 6094–6112.
[81] L. Espinosa-Alonso, A.M. Beale, B.M. Weckhuysen, Acc. Chem. Res. 43 (2010) 1279–1288.
[82] A.V. Neimark, L.I. Kheifez, V.B. Fenelonov, Ind. Eng. Chem. Prod. Res. Dev. 20 (1981) 439–450.
[83] L. Ruffino, R. Mann, R. Oldman, E.H. Stitt, E. Boller, P. Cloetens, M. DiMichiel, J. Merino, Can. J. Chem. Eng. 83 (2005) 132–139.
[84] K.W. Jones, H. Feng, A. Lanzirotti, D. Mahajan, Top. Catal. 32 (2005) 263–272.
[85] L. Seda, A. Zubov, M. Bobak, J. Kosek, A. Kantzas, Macromol. React. Eng. 2 (2008) 495–512.
[86] C.G. Schroer, M. Kuhlmann, T.F. Gunzler, B. Lengeler, M. Richwin, B. Griese-bock, D. Lutzenkirchen-Hecht, R. Frahm, E. Ziegler, A. Mashayekhi, D.R. Haeffner, J.D. Grunwaldt, A. Baiker, Appl. Phys. Lett. 82 (2003) 3360–3362.
[87] J.A. Bergwerff, T. Visser, B.M. Weckhuysen, Catal. Today 130 (2008) 117–125.
[88] A.A. Lysova, I.V. Koptyug, Chem. Soc. Rev. 39 (2010) 4585–4601.
[89] E.K. Gibson, M.W. Zandbergen, S.D.M. Jacques, C. Biao, R.J. Cernik, M.G. O'Brien, M. Di Michiel, B.M. Weckhuysen, A.M. Beale, ACS Catal. 3 (2013) 339–347.
[90] M.W. Zandbergen, S.D.M. Jacques, B.M. Weckhuysen, A.M. Beale, Angew. Chem. Int. Ed. 51 (2012) 957–960.
[91] F. Basile, P. Benito, S. Bugani, W. De Nolf, G. Fornasari, K. Janssens, L. Morselli, E. Scavetta, D. Tonelli, A. Vaccari, Adv. Funct. Mater. 20 (2010) 4117–4126.
[92] A. Zecchina, E. Groppo, S. Bordiga, Chem. Eur. J. 13 (2007) 2440–2460.

[93] A.F. Lee, C.V. Ellis, J.N. Naughton, M.A. Newton, C.M.A. Parlett, K. Wilson, J. Am. Chem. Soc. 133 (2011) 5724–5727.
[94] D.S. Wragg, R.E. Johnsen, P. Norby, H. Fjellvag, Microporous Mesoporous Mater. 134 (2010) 210–215.
[95] C. Guoyong, A. Dagang, L. Chengyue, Catalyst Deactivaton, Elsevier, Amsterdam, 1991.
[96] C.H. Bartholomew, Appl. Catal. A: Gen. 212 (2001) 17–60.
[97] A.M. Beale, E.K. Gibson, M.G. O'Brien, S.D.M. Jacques, R.J. Cernik, M.D. Michiel, P.D. Cobden, Ö. Pirgon-Galin, L.v.d. Water, M.J. Watson, B.M. Weckhuysen, J. Catal. 314 (2014) 94–100.
[98] J. Ruiz-Martinez, A.M. Beale, U. Deka, M.G. O'Brien, P.D. Quinn, J.F.W. Mosselmans, B.M. Weckhuysen, Angew. Chem. Int. Ed. 52 (2013) 5983–5987.
[99] L. Valentini, M.C. Dalconi, M. Parisatto, G. Cruciani, G. Artioli, J. Appl. Crystallogr. 44 (2011) 272–280.
[100] M. Voltolini, M.C. Dalconi, G. Artioli, M. Parisatto, L. Valentini, V. Russo, A. Bonnin, R. Tucoulou, J. Appl. Crystallogr. 46 (2013) 142–152.
[101] J. Nelson, S. Misra, Y. Yang, A. Jackson, Y. Liu, H. Wang, H. Dai, J.C. Andrews, Y. Cui, M.F. Toney, J. Am. Chem. Soc. 134 (2012) 6337–6343.
[102] K. Yakal-Kremski, J.S. Cronin, Y.C.K. Chen-Wiegart, J. Wang, S.A. Barnett, Fuel Cells 13 (2013) 449–454.
[103] A. Fabrizi, S. Ferraro, G. Timelli, Mater. Charact. 85 (2013) 13–25.
[104] P. Zhou, Y. Xia, J. Wang, C. Liang, L. Yu, W. Tang, S. Gu, S. Xu, J. Mater. Chem. B 1 (2013) 685–692.
[105] S. Pani, E.J. Cook, J.A. Horrocks, J.L. Jones, R.D. Speller, Appl. Radiat. Isot. 68 (2010) 1980–1987.
[106] G. Taton, E. Rokita, A. Wrobel, F. Beckmann, P. Thor, M. Worek, World Congress on Medical Physics and Biomedical Engineering, Munich, GERMANY, 2009, pp. 382–385.
[107] S.R. Stock, Int. Mater. Rev. 53 (2008) 129–181.
[108] S.R. Stock, J.D. Almer, J. Appl. Crystallogr. 45 (2012) 1077–1083.
[109] J. Andrieux, C. Chabert, A. Mauro, H. Vitoux, B. Gorges, T. Buslaps, V. Honkimaki, J. Appl. Crystallogr. 47 (2014) 245–255.
[110] C. Steier, A. Madur, H. Nishimura, D. Robin, F. Sannibale, C. Sun, W. Wan, L. Yang, Nucl. Instrum. Methods Phys. Res. Sect. A 649 (2011) 25–29.
[111] P. Varga, A. Pacureanu, M. Langer, H. Suhonen, B. Hesse, Q. Grimal, P. Cloetens, K. Raum, F. Peyrin, Acta Biomater. 9 (2013) 8118–8127.
[112] J. Manickaraj, A. Gorny, Z. Cai, S. Shankar, Appl. Phys. Lett. 104 (2014) (Article No. 073102).
[113] A.M. Beale, M.G. O'Brien, B.M. Weckhuysen, Characterization of Solid Materials and Heterogeneous Catalysts, Wiley-VCH Verlag GmbH & Co. KGaA, Weinheim, Germany, 2012, pp. 1075–1117.
[114] M.A. Newton, W. van Beek, Chem. Soc. Rev. 39 (2010) 4845–4863.
[115] S. Kneip, C. McGuffey, J.L. Martins, S.F. Martins, C. Bellei, V. Chvykov, F. Dollar, R. Fonseca, C. Huntington, G. Kalintchenko, A. Maksimchuk, S.P.D. Mangles, T. Matsuoka, S.R. Nagel, C.A.J. Palmer, J. Schreiber, K.T. Phuoc, A.G.R. Thomas, V. Yanovsky, L.O. Silva, K. Krushelnick, Z. Najmudin, Nat. Phys. 6 (2010) 980–983.
[116] S.M. Hooker, Nat. Photonics 7 (2013) 775–782.
[117] M. Eckert, Ann. Phys. 524 (2012) A83–A85.